Magnetohydrodynamic and Aerodynamic Assessment of Ballistic Entry of a 70° Spherecone at Mars and Venus

Destiny M. Fawley*, Zachary R. Putnam†,
University of Illinois at Urbana-Champaign, Urbana, IL, 61801

Sarah D'Souza‡, Ryan McDaniel§,
NASA Ames Research Center, Moffett Field, CA 94035

and Arnaud Borner¶
AMA, Inc., NASA Ames Research Center, Moffett Field, CA, 94035

An electrical conductivity database for continuum flow in a CO_2 atmosphere over a 70° spherecone was created using the Data Parallel Line Relaxation Code computational fluid dynamics software to inform development of future magnetohydrodynamic subsystems at Venus and Mars. Sixteen freestream conditions were considered at Mars with atmospheric relative velocities from 5 to 8 km/s and altitudes between 20 and 80 km. Sixteen freestream conditions were considered at Venus with atmospheric relative velocities from 9 to 12 km/s and altitudes between 85 and 115 km. Results indicate that the total electrical conductivity in the flow volume always increases as velocity increases. At low velocities, the electrical conductivity is higher at high altitudes, while at high velocities, the electrical conductivity is higher at low altitudes. Three of the 80 km altitude computational fluid dynamics solutions show good agreement with Direct Simulation Monte Carlo results. In general, computational fluid dynamics predicts thinner shocks, higher electron number density, and similar vibrational temperatures as direct simulation Monte Carlo. The magnetohydrodynamic force was calculated at both Mars and Venus. Results indicate there may not be sufficient control authority to use magnetohydrodynamics as a trajectory control mechanism at Mars without artificially increasing the electrical conductivity of the flow, but there may be appreciable control authority for a drag-modulated aerocapture at Venus.

I. Nomenclature

---

*Ph.D. Student, Department of Aerospace Engineering, 104 S. Wright St., AIAA Student Member.

†Assistant Professor, Department of Aerospace Engineering, 104 S. Wright St., AIAA Senior Member.

‡Aerospace Engineer, Entry Systems and Vehicle Development Branch, Moffett Field, CA 94035, AIAA Member

§Aerospace Engineer, Aerothermodynamics Branch, Moffett Field, CA 94035, AIAA Member

¶Senior Research Scientist/Engineer, Thermal Protection Materials and Systems Branch, MS 234-1, Moffett Field, CA 94035, AIAA Member

A = Arrhenius rate coefficient

a = collision cross sectional area, m^2

$\mathbf{B}$ = magnetic field vector, T

B_0 = magnetic field strength at stagnation point, T

c = charge of electron, 1.602×10^{-19} C

E = total energy per unit volume, $\frac{\mathrm{J}}{\mathrm{m}^3}$

e = energy per unit mass, $\frac{\mathrm{J}}{\mathrm{kg}}$

F = force, N

g = acceleration due to gravity on Earth’s surface, $\mathrm{m/s}^2$

h = enthalpy per unit mass, $\frac{\mathrm{J}}{\mathrm{kg}}$

J = diffusion flux, $\frac{\mathrm{kg}}{\mathrm{m}^2\mathrm{s}}$

$\mathbf{j}$ = electric current density vector, $\frac{\mathrm{A}}{\mathrm{m}^2}$

k = reaction rate

k_B = Boltzmann constant, $1.3806 \times 10^{-23} \frac{\mathrm{m}^2\mathrm{kg}}{\mathrm{s}^2\mathrm{K}}$

M = molecular weight, kg

m_e = mass of an electron, 9.109×10^{-31}kg

n = number density, m^{-3}

p = pressure, Pa

$\mathbf{Q}$ = heat flux vector per unit volume, $\frac{\mathrm{W}}{\mathrm{m}^5}$

t = time, s

Q_{T-V} = source term that describes energy transfer between translational and vibrational modes, $\frac{\mathrm{kg}}{\mathrm{s}^3\mathrm{m}}$

R = universal gas constant, $\frac{\mathrm{J}}{\mathrm{mol}\cdot\mathrm{K}}$

R_b = vehicle nose radius, m

$R_{b,r}$ = backward reaction rate coefficient for chemical reaction r

$R_{f,r}$ = forward reaction rate coefficient for chemical reaction r

$\bar{R}$ = average gas constant of gas mixture per unit mass, $\frac{\mathrm{J}}{\mathrm{mol}\cdot\mathrm{kg}\cdot\mathrm{K}}$

r = Arrhenius temperature exponent

s = distance around perimeter of vehicle starting from the stagnation point, m

T = temperature, K

$\mathbf{u}$ = velocity vector, $\frac{\mathrm{m}}{\mathrm{s}}$

V = volume, m^3

X_m = X coordinate offset of magnet, m

x = X coordinate, m

y = Y coordinate, m

α = forward reaction stoichiometric coefficient

β = backward reaction stoichiometric coefficient

ϵ_0 = vacuum permittivity, $8.854 \times 10^{-12}\,\frac{\mathrm{F}}{\mathrm{m}}$

θ = Arrhenius exponential, K

$\nu_{a,b}$ = collision frequency of species a with species b, s^{-1}

ρ = density, $\frac{\mathrm{kg}}{\mathrm{m}^3}$

τ = shear stress, Pa

σ = electrical conductivity, $\frac{\mathrm{S}}{\mathrm{m}}$

Ω = Hall parameter

$\dot{\omega}$ = source term that governs mass production, $\frac{\mathrm{kg}}{\mathrm{s}\cdot\mathrm{m}^3}$

Subscripts

s = chemical species s

r = chemical reaction r

f = forward

b = backward

e = electron

i = ion

v = vibrational

eff = effective

MHD = magnetohydrodynamic

II. Introduction

Magnetohydrodynamics (MHD) is a flow phenomena that has potential application for providing additional deceleration and control of entry vehicles by augmenting the aerodynamic drag with a Lorentz force. During hypersonic flight, high-energy atmospheric gas particles collide in the shock and ionize, creating a locally conductive flow. As the conductive particles cross magnetic field lines, a Lorentz force is exerted on both the charged particles and magnet, as shown in Fig. 1. Studies have shown that the Lorentz drag can be on the same order of magnitude as aerodynamic drag [1–3], and the increased drag allows an entry vehicle to decelerate faster so that supersonic deceleration systems can be deployed at a higher altitude at Mars. Electromagnet technology that allows time-varying magnetic fields may enable

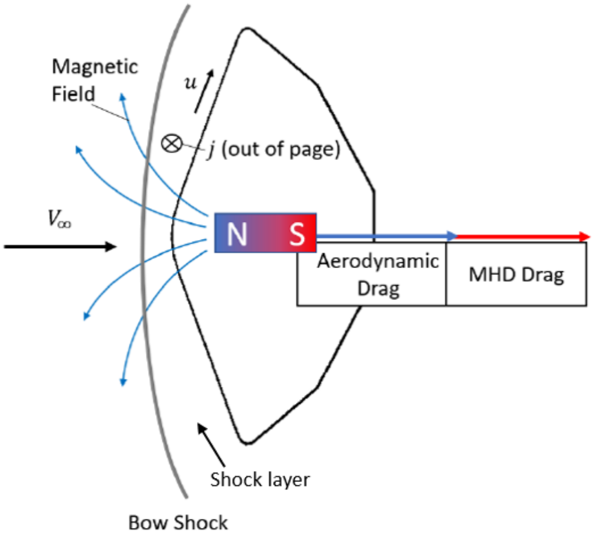

Fig. 1 Diagram of MHD drag on a Mars entry vehicle.

MHD-based drag-modulation trajectory control without jettisoning mass or drag areas. MHD deceleration requires one or more magnets onboard the vehicle to create a magnetic field to generate Lorentz forces. If sufficient forces are generated, the Lorentz forces can be a control mechanism for planetary entry, aerocapture, or aerobraking missions.

MHD has potential applications beyond drag augmentation. The energy from the moving ions may be stored on-board to be utilized for other purposes [4–6]. In-situ resource utilization [7] or gas compression [8] are other possibilities. The Lorentz force on the charged particles also increases the shock thickness, which reduces heat flux to the vehicle [9, 10] and reduces the duration of the communication blackout period [11, 12]. This range of beneficial effects may make MHD an attractive option for future missions.

The effectiveness of MHD depends on the electrical conductivity in the shock layer. A higher conductivity increases the effects of MHD, e.g. the Lorentz force, because there are more ions moving across magnetic field lines. To determine the MHD drag augmentation performance, the electrical conductivity in the flow field must be determined over a range of freestream conditions from atmospheric entry down to about 4 km/s [13].

Several studies have estimated the electrical conductivity in continuum flow, but many make assumptions that may reduce the accuracy of the estimated MHD force. Some studies used analytical models to estimate the MHD drag [14–16]. Others used a 1-dimensional shock solver to determine the electrical conductivity directly behind the shock and assumed constant properties throughout the shock [5, 15, 17]. Other studies used the Navier-Stokes equations, Maxwell equations, and Ohm's Law to solve for the electrical conductivity in the flowfield [1, 6, 18–23]. This method relies on fewer assumptions about the flow electrical conductivity compared to 1-dimensional solvers or analytical equations, and it provides the most accurate representation of physical phenomena with the capabilities of current simulation tools. However, due to the computational cost of MHD simulations, studies are limited to single point designs or geometries that are impractical for entry. Additionally, the results are specific to the freestream conditions, magnet strength, and magnet placement that were used in the studies. To estimate the MHD force over an entire trajectory, many simulations must be done at a range of freestream velocities and densities. Any change in the magnet would warrant further simulations to estimate how the flowfield properties change over the range of freestream conditions that the vehicle encounters.

The goal of this study is to document the electrical conductivity over a range of altitudes and velocities in a CO_2 atmosphere to inform future studies. The computational fluid dynamics (CFD) solutions in this study do not include the generalized Ohm's Law for coupled MHD-flow effects. Previous studies have shown that the presence of a magnetic field has little effect on the electrical conductivity profile in the shock [21, 24]. The shock standoff distance can be sensitive to magnetic field strength, with the shock standoff increasing up to a factor of 8 for a magnetic field strength of 0.5 T [23]. At high densities, the shock standoff distance does not change as much from MHD effects. Even though the shock standoff distance cannot be accurately predicted without the Maxwell equations and Ohm's Law, the MHD force may be estimated because the electrical conductivity magnitude in the shock is similar when an external magnetic field is applied and when there is not magnetic field [24]. The results from this study may save significant computational resources and time by providing an estimate of the MHD force for a wide variety of magnetic field configurations without solving the Maxwell equations each time.

The MHD force for several conditions is calculated and compared with existing literature. Furthermore, a comparison between CFD and Direct Simulation Monte-Carlo (DSMC) for a few overlapping conditions from a previous study is presented [25]. Finally, the MHD force is calculated over a range of altitudes and velocities at both Mars and Venus. The force calculation provides an estimate of the MHD force one could expect with similar conditions.

III. CFD Freestream Selection

Several example aeroassist trajectories were computed at both Venus and Mars to determine the range of conditions that may be encountered during flight. The composition of both atmospheres are similar. Mars' atmosphere is approximately 95% CO_2 while Venus' atmosphere is approximately 96% CO_2. Because their compositions are so similar, CFD results may be applied to either planet; however, Venus arrival velocities (10-12 km/s) are typically higher than Mars arrival velocities (4-6 km/s). Four mission classes were considered for Mars: a Mars Phoenix-sized vehicle with a ballistic coefficient of 65 kg/m^2 and diameter of 2.6 m [26], a Mars Science Lab-sized vehicle with a ballistic coefficient of 120 kg/m^2 and diameter of 4.5 m [26], a human-class vehicle with a ballistic coefficient of 234 kg/m^2 and a diameter of 16 m, and a human-class vehicle with a ballistic coefficient of 415 kg/m^2 and diameter of 16 m. Two Venus missions are considered with ballistic coefficients of 50 kg/m^2 and 150 kg/m^2 and diameters of 3 m and 1.7 m, respectively. The two Venus missions correspond to small and large orbiters performing aerocapture.

All Martian entry vehicles are assumed to be unguided with a 0° trim angle of attack. Although MSL was a lifting vehicle, the lift-to-drag ratio is set to 0 to make the trajectory similar to that of a drag-modulated control scheme that could be provided by MHD. The goal of the trajectory analysis was to determine the altitude band at which a vehicle of each size would have a velocity above 5 km/s. Below 5 km/s, there is not enough ionization to produce sufficient MHD effects, so it is not considered in the CFD run matrix. Entry conditions for the Phoenix and MSL class vehicles were the same as their respective missions except for the flight-path angle, which was modified to be in the entry corridor for the modified lift-to-drag ratio. The flight-path angle for both vehicles was -10°.

Several studies have analyzed human Mars missions with constraints on mission time, which may be necessary for human health. Human missions may require higher entry velocities than previous robotic missions due to the mission time constraints. Shorter mission times generally lead to higher entry velocities. The literature indicates that a human mission may have an entry velocity between 6-9 km/s [27–30] and an entry mass between 20,000-80,000 kg [27, 31, 32]. Two human-class missions were selected for the trajectory analysis: an 80,000 kg vehicle with an entry velocity of 6 km/s and a 20,000 kg vehicle with an entry velocity of 7.8 km/s. An entry velocity of 7.8 km/s for the lighter vehicle was chosen because it is the maximum entry velocity that allows aerocapture without going over the 5*g* acceleration limit with a ballistic entry, a proxy for the maximum allowable acceleration of a human mission. The two selected human missions provide approximate bounds on the range of trajectories for a human mission. The notional human-class vehicle uses a 70° spherecone forebody with a 16 m diameter, which may be possible with future inflatable technology such as the hypersonic inflatable aerodynamic accelerator (HIAD). The human mission performs an aerocapture maneuver in the first atmospheric pass, which is consistent with the concept of operations suggested by literature [31, 33]. The entry flight-path angle was chosen to target an apoapsis of 17,500 km while keeping peak acceleration under 5*g* [34, 35].

The altitude-velocity curves for the four Martian trajectories are plotted in Fig. 2. The MSL and Phoenix missions are above 5 km/s when their altitudes are above 40 km. The 80,000 kg human aerocapture trajectory has a minimum altitude of 32 km at a velocity of 5 km/s. The 20,000 kg human mission has a minimum altitude of 43 km at a velocity of 5.7 km/s. From the trajectories shown, the CFD should capture altitudes above 32 km and velocities between 5 km/s and 8 km/s.

Next, the 50 kg/m^2 and 150 kg/m^2 aerocapture missions were simulated at Venus. Venus entry velocities are typically between 10 km/s and 12 km/s [36, 37]. An entry velocity of 11.5 km/s was selected for this study. The entry flight-path angle was selected to target an apoapsis of 1,720 km for both missions. The Venus trajectories are shown in Fig. 2. The minimum altitude is approximately 100 km.

The Mars and Venus trajectories described above determined the conditions at which CFD will be run. At Mars, velocities between 5-8 km/s and altitudes above 30 km must be considered. Because the Navier-Stokes equations are not valid for transitional or rarefied flow, that maximum altitude is limited to 80 km with a Knudsen number of 0.005.

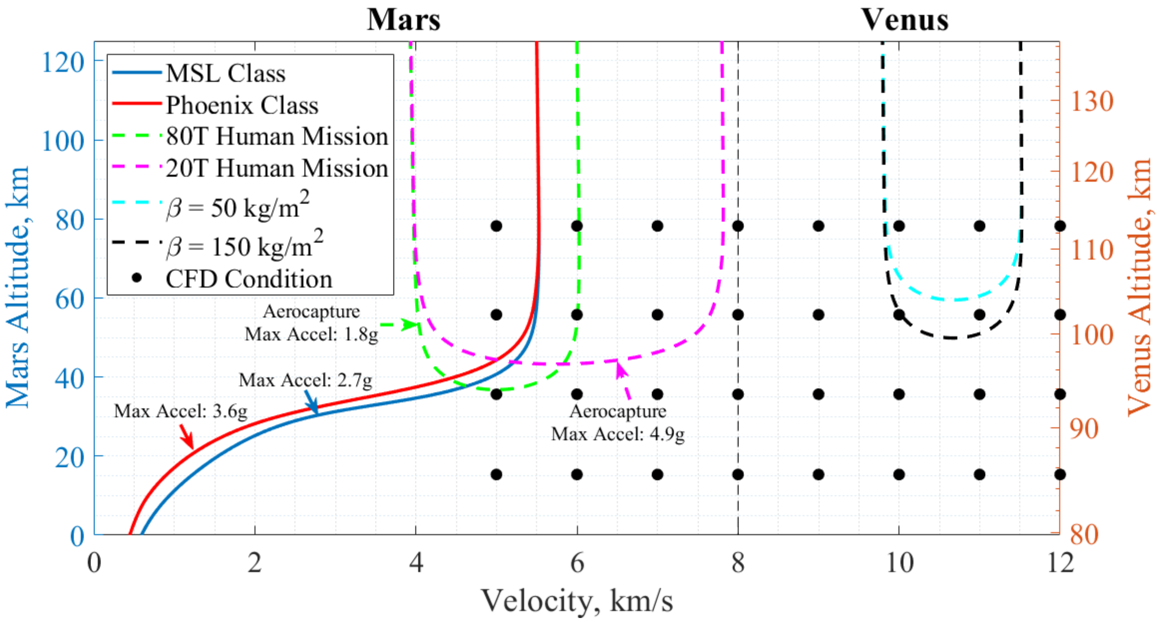

Fig. 2 Altitude-velocity trajectories for Phoenix, MSL, and human class missions at Mars. The black dots indicate the CFD test matrix.

The altitude envelope that will be considered in this study was expanded to 20-80 km to capture variations in future trajectories that may cause the minimum altitude to go below 30 km. For Venus, velocities between 9.8-11.5 km/s and altitudes between 100-115 km should be considered. Both the velocity and altitude envelopes were expanded to capture variations in the trajectories due to different control mechanisms. At Venus, velocities between 9-12 km/s and altitudes between 85-115 km were chosen for evaluation with CFD. The selected range of conditions can provide a database of electrical conductivity that could be used for many future trajectory missions.

IV. Methods and Assumptions

A. Freestream Conditions

At Mars, velocities between 5-8 km/s and altitudes between 20-80 km ($\rho \in [2.15 \times 10^{-6}, 3.21 \times 10^{-3}]$ kg/m^3) are covered in the electrical conductivity database. The CFD conditions were selected to cover every 1 km/s and every 20 km. This spacing provides sufficient data points with which to interpolate the MHD force for most trajectories of interest while balancing computational cost. Figure 2 shows all the CFD simulation conditions at Mars.

The Venus electrical conductivity database covers velocities from 9-12 km/s in intervals of 1 km/s. The altitude range is 85-115 km ($\rho \in [2.15 \times 10^{-6}, 3.21 \times 10^{-3}]$ kg/m^3) in intervals of approximately 8 km. Figure 2 shows all the CFD simulation conditions at Venus. Note that the freestream atmospheric density is the same between Mars and Venus at each altitude band.

For all cases, the freestream temperature is assumed to be 140.3 K. The freestream contains mole fractions of 0.9573

CO_2 and 0.0427 N_2. The composition does not change with altitude. The mole fractions do not exactly match the composition of both atmospheres, which vary over time and altitude. The assumed composition is an approximation that is very close to the recorded composition of both planets.

B. Vehicle Geometry

The vehicle geometry considered for this study is based on the Mars 2020 entry vehicle [38]. The 70° spherecone geometry is selected due to heritage of previous Mars lander missions. The dimensions are given in Fig. 3. The forebody is a 70° spherecone with a nose radius of 2.5 m. A vehicle diameter of 10 m is considered. The dimensions of the Mars 2020 vehicle are scaled to reach the desired size while maintaining the same aspect ratio.

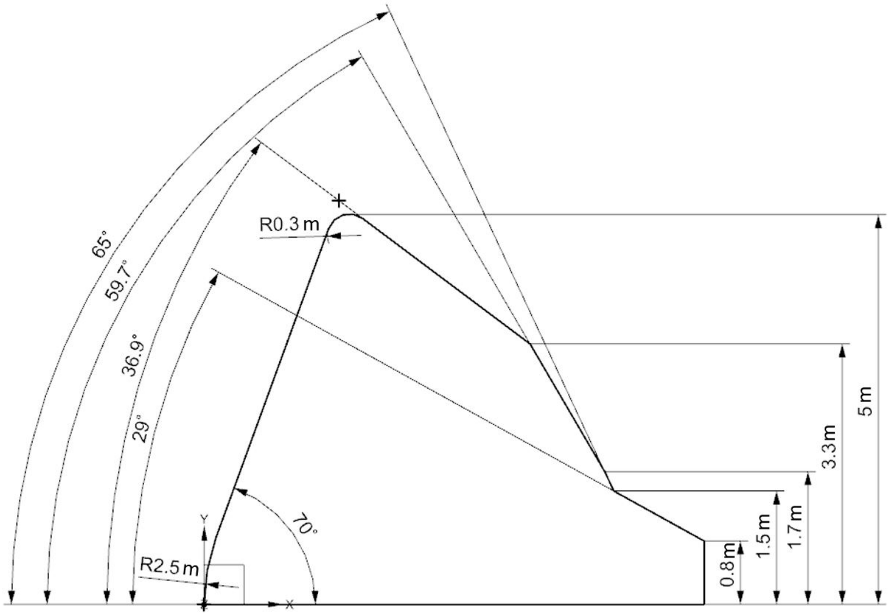

Fig. 3 Mars 2020 aeroshell geometry scaled to a 10 m diameter [38].

C. Magnetic Field

The magnet configuration considered in this study is a single dipole magnet as in [23]. The equation for a dipole magnet is:

$$B(x, y, z) = -\frac{B_0 X_m^3}{2} \left[\frac{3\mathbf{r}(\mathbf{m} \cdot \mathbf{r})}{r^5} - \frac{\mathbf{m}}{r^3} \right]^T, \tag{1}$$

where **m** is the magnet axis and **r** is the probing location for the magnetic field. Both **m** and **r** are defined as:

$$\mathbf{r} = \begin{bmatrix} x - X_m & y & z \end{bmatrix}^T; \qquad \mathbf{m} = \begin{bmatrix} 1 & 0 & 0 \end{bmatrix}^T \tag{2}$$

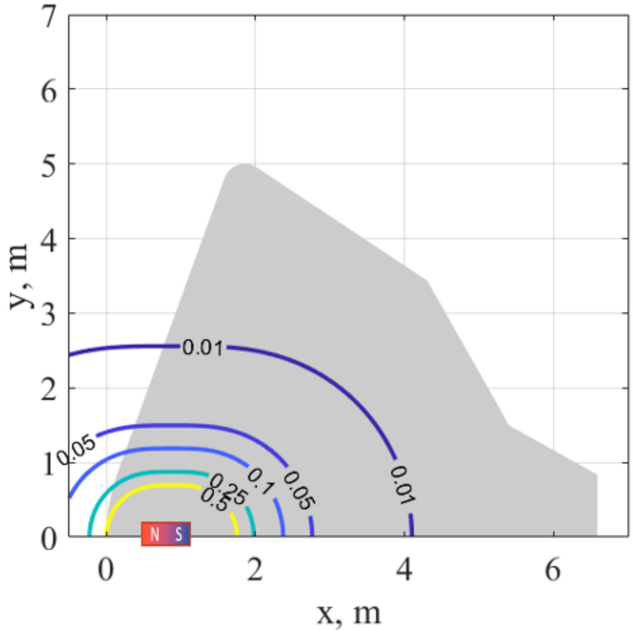

Fig. 4 Contours of magnetic field strength in T. The magnet is located at (0.875,0) and scaled to have a magnetic field strength of 0.5 T at the stagnation point.

The magnet has no thickness and is located at (0.875,0) m inside the vehicle. Because the magnet is offset from $x = 0$, the factor X_m is included in the magnetic field equation and has a value of 0.875 m. The vector $\mathbf{m}$ is the vector along the magnet axis, which points along the x-axis. The magnet strength is scaled to have a stagnation point magnetic field strength $B_0 = 0.5$ T. The magnet configuration is shown in Fig. 4.

D. Numerical Methods

The Data Parallel Line Relaxation Code (DPLR) [39] software was used to solve the laminar full Navier-Stokes equations with a 2-dimensional axisymmetric grid. Seventeen species are included in the simulation, including CO_2, CO, CO^+, C_2, N_2, O_2, O_2^+, NO, NO^+, CN, C, C^+, N, N^+, O, O^+, and e^-. The flow is assumed to be in thermal, chemical, and vibrational non-equilibrium. Rotational energy is assumed to be in equilibrium with translational energy. The electronic and free electron temperatures are in equilibrium with vibrational temperature. Radiation is neglected.

The conservation equations are solved as noted in the DPLR manual [39]. The conservation of mass of each species s is given by:

$$\frac{\partial \rho_s}{\partial t} + \nabla \cdot (\rho_s \mathbf{u} + \mathbf{J}) = \dot{\omega}_s \tag{3}$$

In the conservation of mass, $\dot{\omega}_s$ is a source term the governs the mass production of species s, and it is calculated as:

$$\dot{\omega}_s = M_s \sum_{r=1}^{35} \left(\beta_{s,r} - \alpha_{s,r}\right) \left(R_{f,r} - R_{b,r}\right). \tag{4}$$

The forward and backward reaction rate coefficients are:

$$R_{f,r} = k_{f,r} \prod_{s=1}^{17} \left(\rho_s/M_s\right)^{\alpha_{s,r}}, \quad R_{b,r} = k_{b,r} \prod_{s=1}^{17} \left(\rho_s/M_s\right)^{\beta_{s,r}} \tag{5}$$

The forward and backward reaction rates are calculated with the Arrhenius equation:

$$k = AT^{r} \exp\left(-\theta/T\right) \tag{6}$$

Arrhenius parameters are taken from Johnston et al. [40]. There are 35 chemical reactions, which are described in Appendix A. Equilibrium constants are computed from NASA Lewis fits [40]. All reactions are reversible. The total energy per unit volume equation is:

$$\frac{\partial E}{\partial t} + \nabla \cdot \left[\left(E + p\right)\mathbf{u}\right] + \nabla\left(\tau \cdot \mathbf{u}\right) + \nabla \mathbf{Q} - \nabla \cdot \sum_{s=1}^{ns} h_s J_s = 0 \tag{7}$$

Finally, there is one equation for each internal energy mode. Because rotational energy is in equilibrium with translational energy, a separate equation is not necessary for the rotational mode. Vibrational energy is in equilibrium with electronic and free electron energy, so there is only one equation for vibrational energy per unit volume:

$$\frac{\partial E_v}{\partial t} + \nabla\left(E_v \mathbf{u}\right) + \nabla \cdot \mathbf{Q}_v + \nabla \cdot \sum_{s=1}^{ns} \rho_s e_{vs} \mathbf{v}_s = \sum_{s=1}^{ns} \dot{\omega}_s e_{vs} + Q_{T-V} \tag{8}$$

where Q_{T-V} is a source term that describes energy transfer between translational and vibrational modes. The final equation is the state equation assuming an ideal gas:

$$p = \sum_{s=1}^{ns} \rho_s \bar{R} T, \quad \text{where} \quad \bar{R} = \sum_{s=1}^{ns} \frac{\rho_s}{\rho} \frac{R}{M_s} \tag{9}$$

Formation enthalpies of NO, NO^+, N, and O are from Candler [41] while the rest are from Gurvich et al. [42]. Characteristic vibrational temperatures of N_2, O_2, and NO are from Candler [41]. All other characteristic vibrational temperatures, in addition to most characteristic electronic temperatures, are from Gurvich et al. [42]. Characteristic electronic temperatures of C, C^+, N, N^+, O, O^+, and e^- are from the NIST online database [43]. Transport properties are calculated with Gupta's fit [44] with Yos approximate mixing rules. Transport properties are from a variety of different sources [45–59], which are all cited in DPLR. Thermodynamic properties of each species are from McBride [60]. Vibrational relaxation times follow the Millikan-White expression [61] with the correction suggested by Park [62].

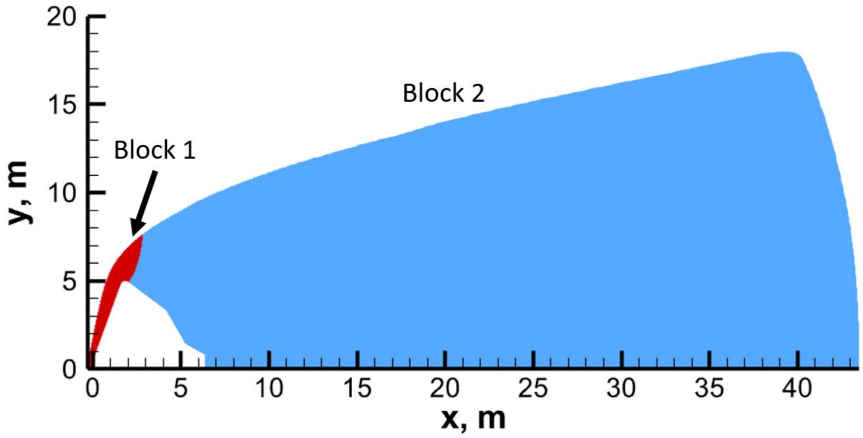

Fig. 5 An example grid with two blocks highlighted.

The vehicle surface is a radiative equilibrium wall with a constant emissivity of 0.85.

A 2-dimensional axisymmetric simulation is used to reduce computational cost without fundamentally changing the results compared to a 3-dimensional simulation. The grid is split into two blocks to improve grid adaption and decrease computation time. The first block has 160 nodes in the body-normal direction and 536 points along the body surface. The second block has 160 points in the body-normal direction and 312 points along the body surface. Once an initial converged solution is reached, the grid adaption feature in DPLR is utilized to move the outer grid boundary near the shock to achieve higher resolution in the shock layer. At least three grid adaptions are completed for each freestream case to ensure a high-quality grid. An example grid with the two blocks highlighted is shown in Fig. 5.

E. MHD Force Calculation

The MHD force is calculated as:

$$\mathbf{F_{MHD}} = \iiint_V \mathbf{j} \times \mathbf{B} \, dV \tag{10}$$

where **j** is the electric current density vector. Any electric field is assumed to be negligible, so

$$\mathbf{j} = \sigma_{\text{eff}} \left(\mathbf{u} \times \mathbf{B} \right) \tag{11}$$

The force becomes:

$$\mathbf{F_{MHD}} = \iiint_V \sigma_{\text{eff}} \left(\mathbf{u} \times \mathbf{B} \right) \times \mathbf{B} dV \tag{12}$$

Note that the Maxwell equations and Ohm's Law were not included in the CFD solver. Even though there is no electric current density in the solution, the **j** vector is estimated by superimposing the external magnetic field onto the flowfield solution. By keeping the CFD and magnetic field uncoupled, the force for all 32 freestream conditions can be calculated by solving a few analytic equations. The uncoupled method is computationally cheaper than numerically solving a coupled Navier-Stokes Maxwell Equation problem for every magnetic field of interest at each freestream condition. Several results of the uncoupled method are compared with coupled simulations in literature to estimate error in the force calculation.

The triple integral in Eq. (12) is approximated as the sum of the integrand in each cell of the CFD grid revolved around the x-axis. The cell volume and flow velocity are taken directly from the CFD solution.

Previous studies have shown that the Hall effect significantly reduces the electric current density magnitude at densities that are equivalent to 40 km at Mars and higher [24]; therefore, the Hall and ion slip effects are accounted for in the electrical conductivity post-processing. The effective electrical conductivity σ_{eff} is the electrical conductivity corrected for Hall and ion slip effects [6, 63]:

$$\sigma_{\text{eff}} = \frac{\tilde{\sigma}}{1 + \tilde{\Omega}^2} \tag{13}$$

$$\tilde{\sigma} = \frac{\sigma}{1 + \Omega_e \Omega_i}; \quad \tilde{\Omega} = \frac{\Omega_e}{1 + \Omega_e \Omega_i} \tag{14}$$

$$\Omega_e = \frac{cB}{m_e \left(\nu_{ei} + \nu_{en}\right)}; \quad \Omega_i = \frac{cB}{M \nu_{in}} \tag{15}$$

The electrical conductivity of the flow is given by [21, 22]:

$$\sigma = \frac{n_e c^2}{m_e \sum_{s \neq e} \nu_{es}} \tag{16}$$

with the collision frequency of electrons with species s:

$$\nu_{es} = \begin{cases} 6\pi \left(\dfrac{c^2}{12\pi\epsilon_0 k_B T_{ve}}\right)^2 \ln\left[12\pi\left(\dfrac{\epsilon_0 k_B}{c^2}\right)^{3/2}\sqrt{\dfrac{T_{ve}^3}{n_e}}\right] n_s \sqrt{\dfrac{8 k_B T_{ve}}{\pi m_e}} & \text{if s is ion species} \\ \dfrac{4}{3} a_{e,s} n_s \sqrt{\dfrac{8 k_B T_{ve}}{\pi m_e}} & \text{otherwise} \end{cases} \tag{17}$$

The effective electrical conductivity is dependent on the magnetic field. For generality, the flow electrical conductivity σ is reported in the results, but all force calculations in Section V.E use the effective electrical conductivity with the magnet configuration given in Section IV.C. Because the electrical conductivity reported in Section V is independent of magnetic field, future studies could assume a different magnetic field configuration and recalculate the MHD force.

V. Results

A. Convergence Assessment

Several checks were completed to ensure each case fully converged. Each solution was checked for reasonable temperature profiles and chemistry, relative magnitudes of stagnation line and forebody-normal quantities, and surface quantities. Only the 12 km/s, 20 km case is shown here to demonstrate the quality checks; however, the the quality checks were applied to all CFD solutions.

The Mach number, translational temperature, and vibrational temperature are given in Fig. 6. The Mach contour in Fig. 6a shows where the shock is located. The outer boundary is adapted to follow the shock closely, so the grid can capture more detail in the shock layer. Additionally, a check was done to ensure at least two freestream points are present along the outer boundary so that the shock solution is not cut off. The translational temperature in Fig. 6b reaches a peak value of 17,000 K in the shock on the stagnation line and decreases to approximately 12,500 K in the shock layer. Finally, the vibrational temperature in Fig. 6c does not have a distinct peak, but it increases to approximately 13,000 K in the shock layer. The vibrational temperature does not have a peak because it takes more time to excite vibrational modes of a molecule. The grid is adapted well and the temperature contours show expected trends.

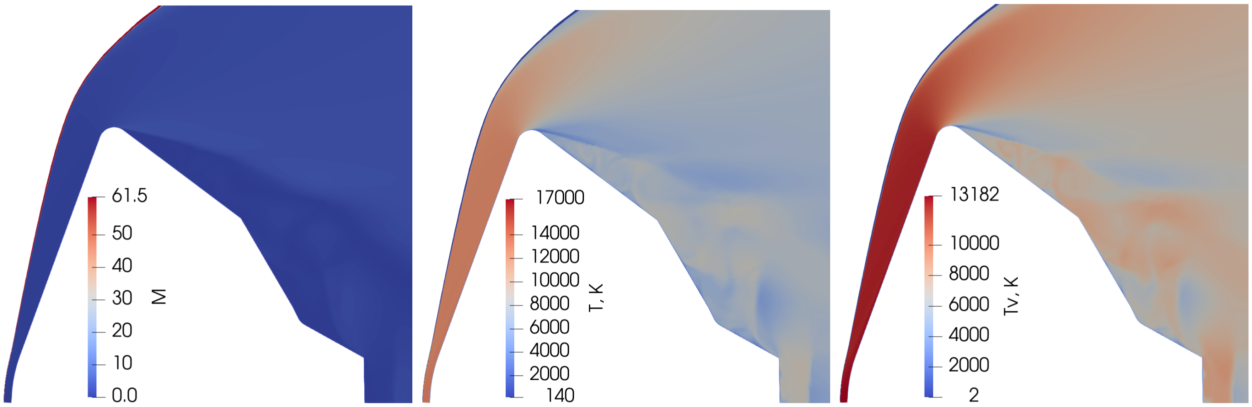

a) **b)** **c)**

Fig. 6 Contour plots of the a) Mach number, b) temperature, and c) vibrational temperature at 20 km Mars altitude with a velocity of 12 km/s.

Figure 7 has contours for CO_2, CO, O_2, and O mole fractions. At 12 km/s, nearly all molecules would dissociate [64], which is demonstrated in Fig. 7a, b, and c. In the wake where the flow has cooled, the atoms begin to recombine into CO. There is not an appreciable amount of CO_2 or O_2 in the flow near the vehicle.

Next, several quantities were compared between the stagnation line and mid-forebody line. The lines traced out by the two locations are highlighted in Fig. 8a. The temperature and vibrational temperature are compared in Fig. 8b. The vehicle surface is located at $s_j = 0$, the stagnation line shock is at $s_j = 0.13$, and the midbody shock is at $s_j = 0.46$. The shock is significantly thicker at the mid-forebody than at the stagnation line. The stagnation line also has slightly

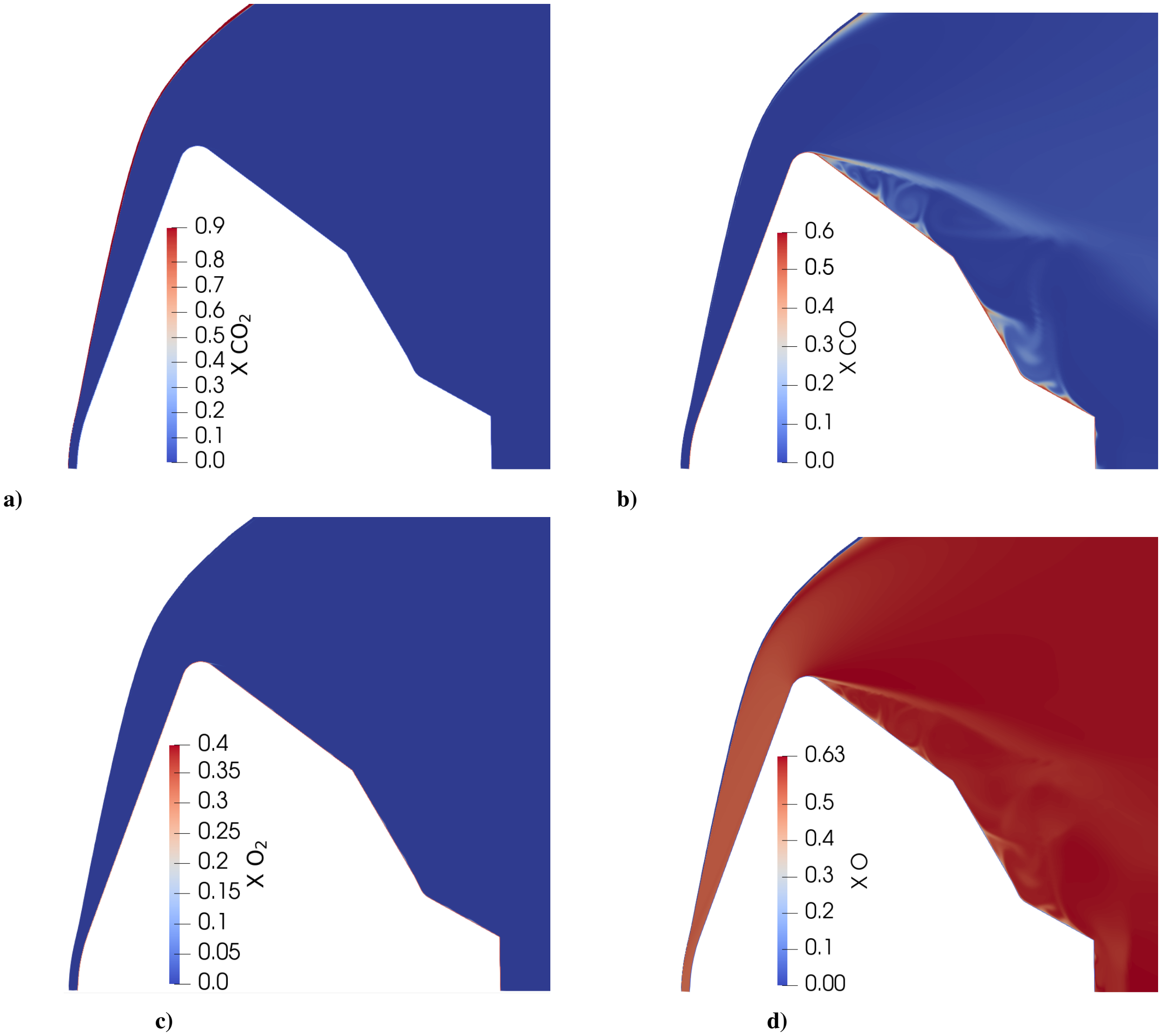

Fig. 7 Contour plots of mole fractions of a) CO_2, b) CO, c) O_2, and d) O at 20 km with a velocity of 12 km/s at Venus.

higher vibrational and translational temperatures. The chemical composition is shown in Fig. 8c. Both the stagnation line and midbody line are almost completely dissociated; however, the midbody line has slightly higher mole fractions of CO, CO_2, and O_2. The midbody line has a lower temperature than the stagnation line, indicating some recombination. Finally, the electron number density is compared at the two locations. The stagnation line has significantly higher e^-number density due to the higher temperature and lower velocity.

Several surface quantities were inspected for expected trends and orders of magnitude. The vehicle surface is parameterized by s, the distance along the 2-dimensional perimeter starting from the stagnation point. That is, s = 0 m on the nose and the maximum value s = 12.8 m occurs at the back of the vehicle. The parameterization is shown in Fig. 9.

The surface temperature is shown in Fig. 10a. The temperature is highest at the stagnation point (s = 0 m), then it decreases rapidly over the spherical portion of the spacecraft. The temperature continues decreasing nearly linearly until the shoulder at $s = 5$ m. The surface temperature is very noisy behind the shoulder due to turbulence. Turbulence modeling was not required because the shock layer is laminar. The wake is not relevant to this study because there is insufficient ionization behind the shoulder to significantly change the MHD force. The surface pressure is shown in Fig. 10b. The pressure is highest at the stagnation point, is approximately constant along the frustum, then drops behind the shoulder. The pressure follows the expected behavior for hypersonic flight. The surface heat flux is shown in Fig 10c. There is a small jump at the stagnation point due to the axisymmetric boundary condition. Because there is only one point out of family, it does not affect the electrical conductivity results shown later as they are dependent on volumetric properties. Overall, the heat flux has expected behavior with peaks on the nose and shoulder. The shoulder peak is steeper because the radius is smaller. Finally, the surface shear is shown in Fig. 10d. The shear is maximum at the shoulder where the flow has a high velocity tangent to the surface. All surface quantities have expected trends, indicating the solution is fully converged and reasonable.

B. DSMC and CFD Comparison

DSMC methods and results with similar flow conditions to those considered in this study are presented in [25]. In the previous study, the 6, 7, and 8 km/s velocities at 80 km Mars altitude were run with the Stochastic PArallel Rarefied-gas Time-accurate Analyzer (SPARTA). The freestream conditions are the same as the DPLR cases in this study, but DPLR has a catalytic radiative equilibrium wall boundary condition while SPARTA uses a catalytic isothermal wall with fully diffuse collisions. The following comparison between the two solutions at these three conditions bridges rarefied and continuum electrical conductivity models. Code-to-code verification also improves confidence in the solutions.

The Mach contours for the 6, 7, and 8 km/s comparison cases are shown in Fig. 11. All three cases predict a much wider shock with DSMC. The Knudsen number at this condition is 0.005, which is close to transitional flow. The Navier-Stokes equations may not be as accurate as the Boltzmann equation at these conditions. Additionally, the different boundary conditions may contribute to the difference in shock width.

The Boltzmann equation is more accurate than the Navier-Stokes equations when there are enough particles to get good averages in the flow. The DSMC results are better in the shock where the particle density is high, but they may not be as accurate in the wake where there are too few trace species to get a reasonable electrical conductivity estimate. The Navier-Stokes equations are less accurate in these cases that are near the transitional regime (Kn = 0.005), particularly in the wake where the flow is less dense than in the shock and the flow is turbulent. For a full electrical conductivity model that includes both rarefied and continuum flow, the DSMC results in the shock layer should be trusted more at 80 km and above. Below approximately 80 km, the flow is to be continuum, and DPLR can be used. All points in the CFD run matrix for this research are 80 km or below.

The vibrational temperature is shown in Fig. 12. The vibrational temperature is similar between the two solution sets. DSMC estimates a higher vibrational temperature throughout the shock layer with the peak close to the shoulder. CFD has the peak temperature just behind the shock near the nose of the vehicle. The two solution sets agree more at higher velocities (8 km/s) then at low velocities (6 km/s).

The electron number density is given in Fig. 13. The electron profile looks similar between SPARTA and DPLR for all cases; however, DPLR predicts significantly higher electron number density for both the 8 km/s and 6 km/s cases. Both solutions agree well at 7 km/s. The difference may be due to the shock width difference. DPLR has a smaller shock layer, so the post-shock density is higher. More collisions allow the chemistry to equilibrate faster, causing more particles to ionize.

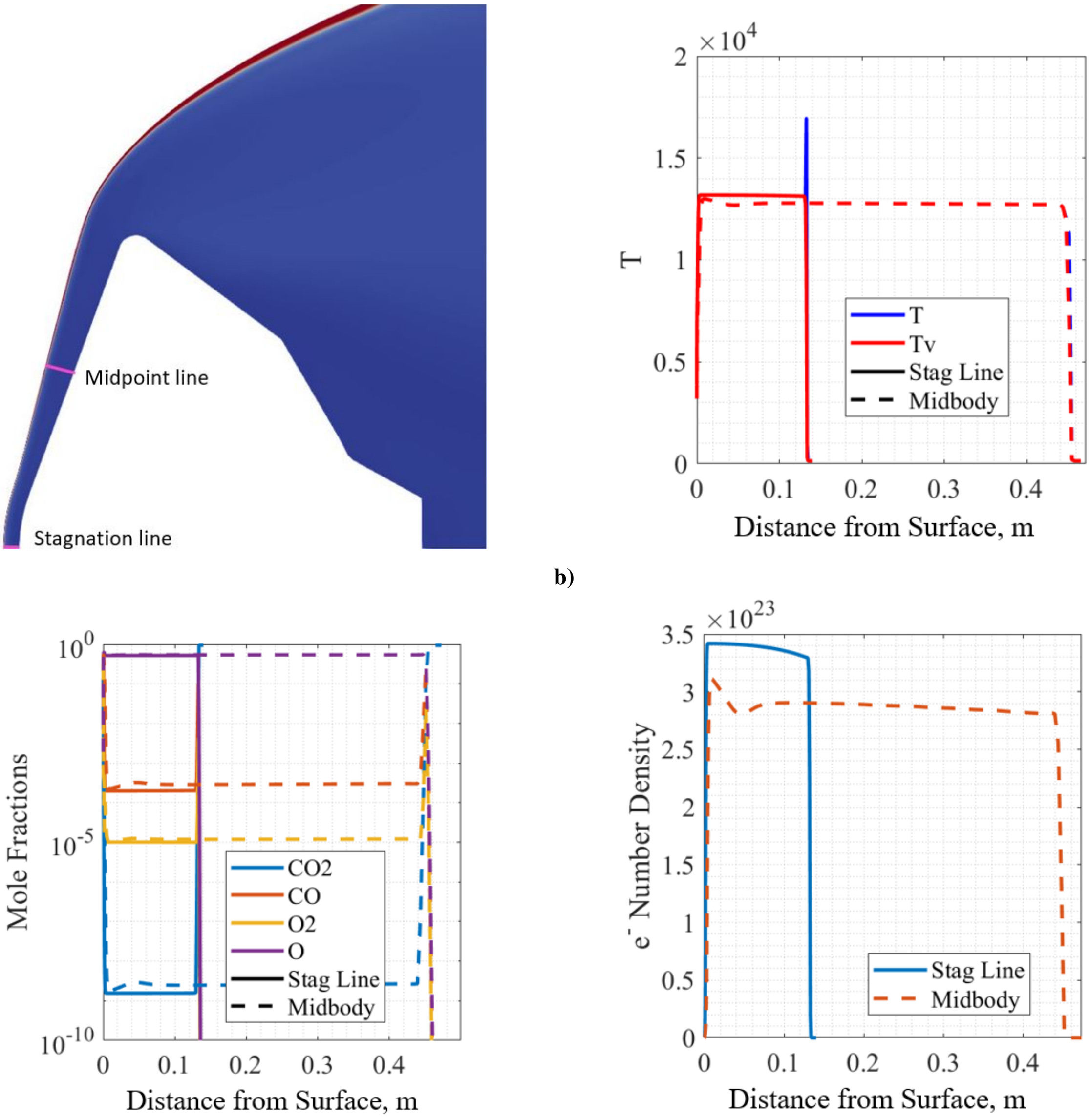

a)

b)

c)

d)

Fig. 8 The stagnation line and midbody lines are shown in a). The b) translational and vibrational temperatures, c) species mole fractions, and d) electron number densities are compared along both lines from the vehicle surface ($s_j = 0$) to the shock at 20 km with a velocity of 12 km/s.

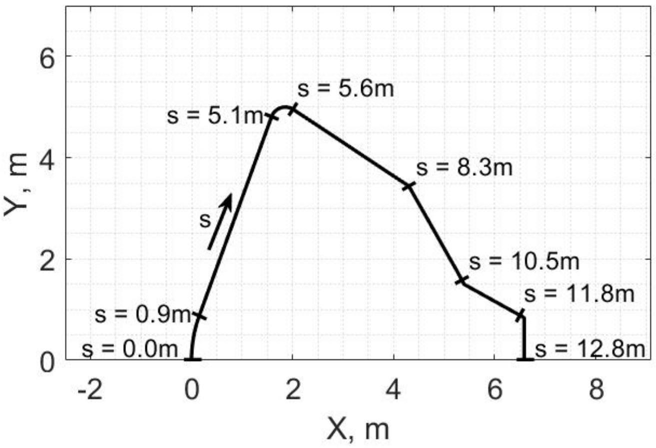

Fig. 9 Parameterization s of the vehicle's surface.

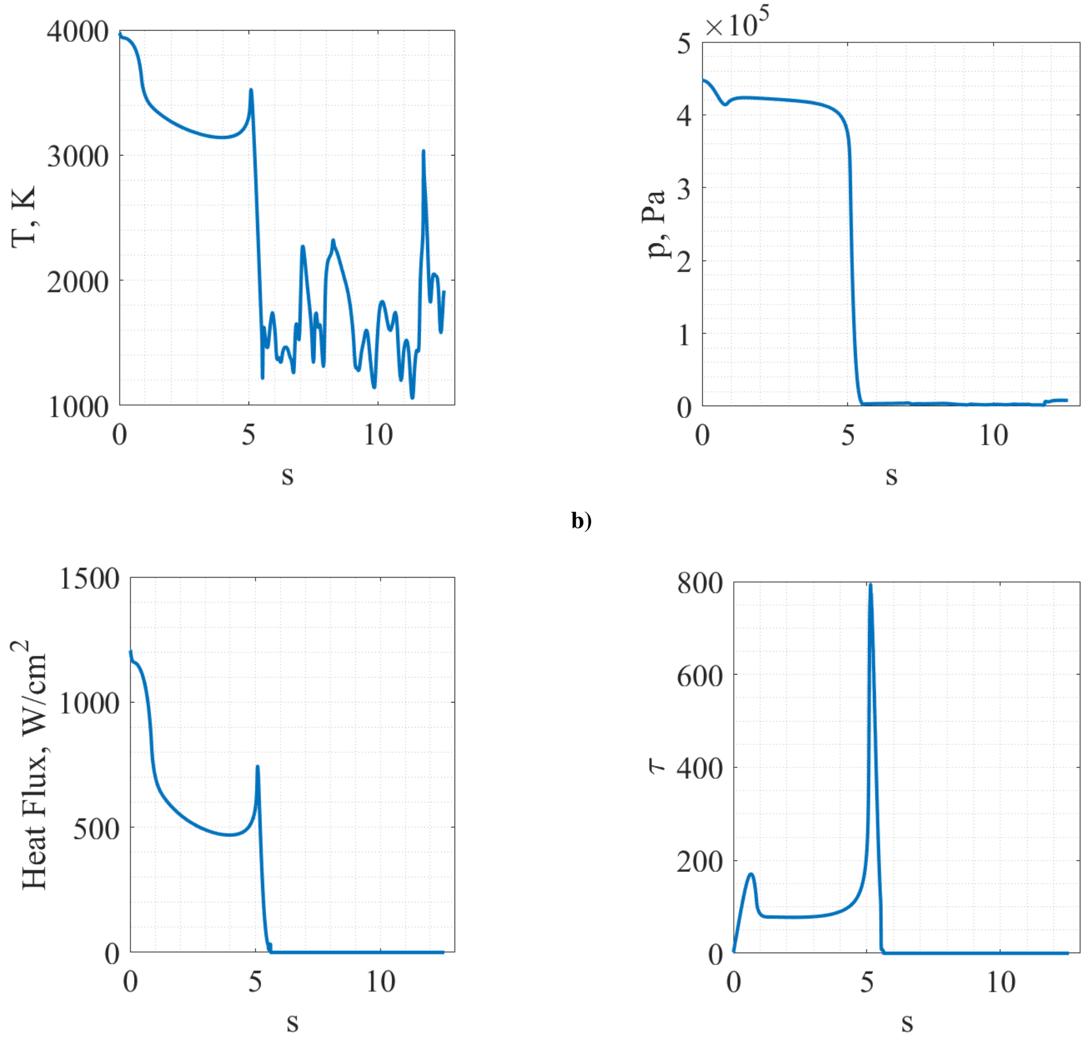

a) **b)** **c)** **d)**

Fig. 10 The surface a) temperature, b) pressure, c) heat flux, and d) shear stress from the stagnation point ($s = 0$ m) to the back of the vehicle ($s = 12.6$ m) at 20 km with a velocity of 12 km/s.

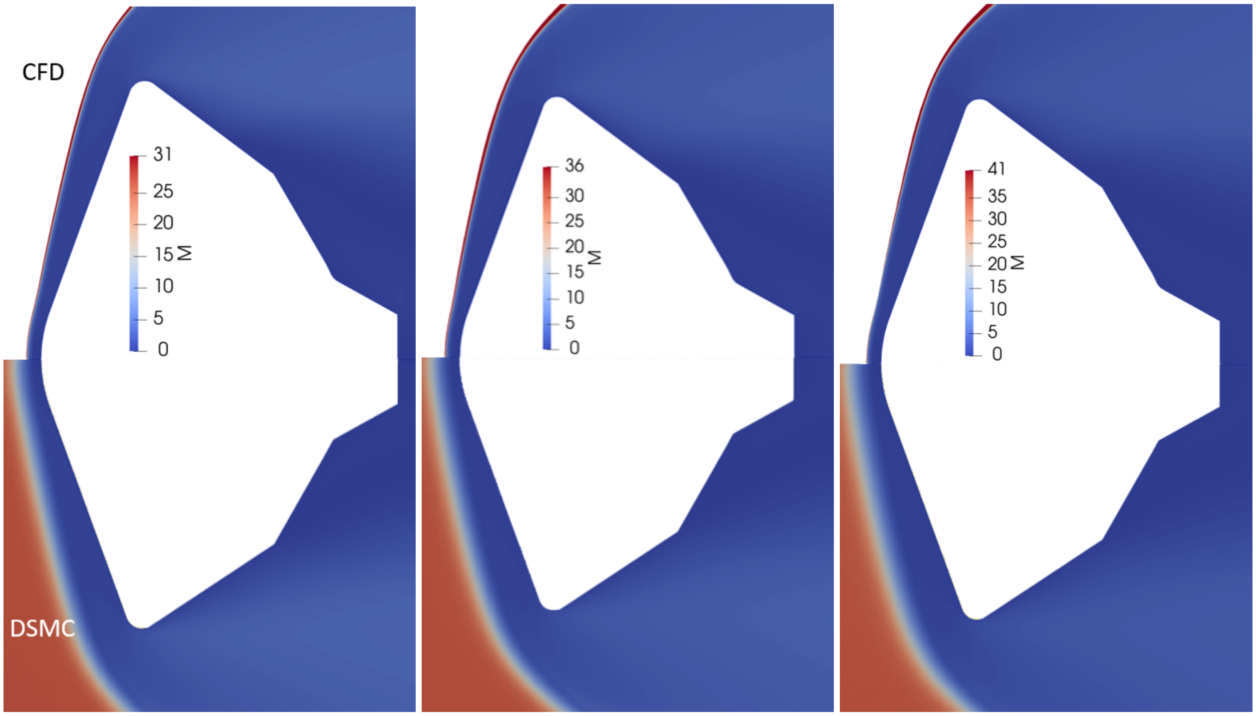

a) b) c)

Fig. 11 Mach contour CFD and DSMC comparison at 80 km at Mars with a) 6 km/s, b) 7 km/s, and c) 8 km/s velocities.

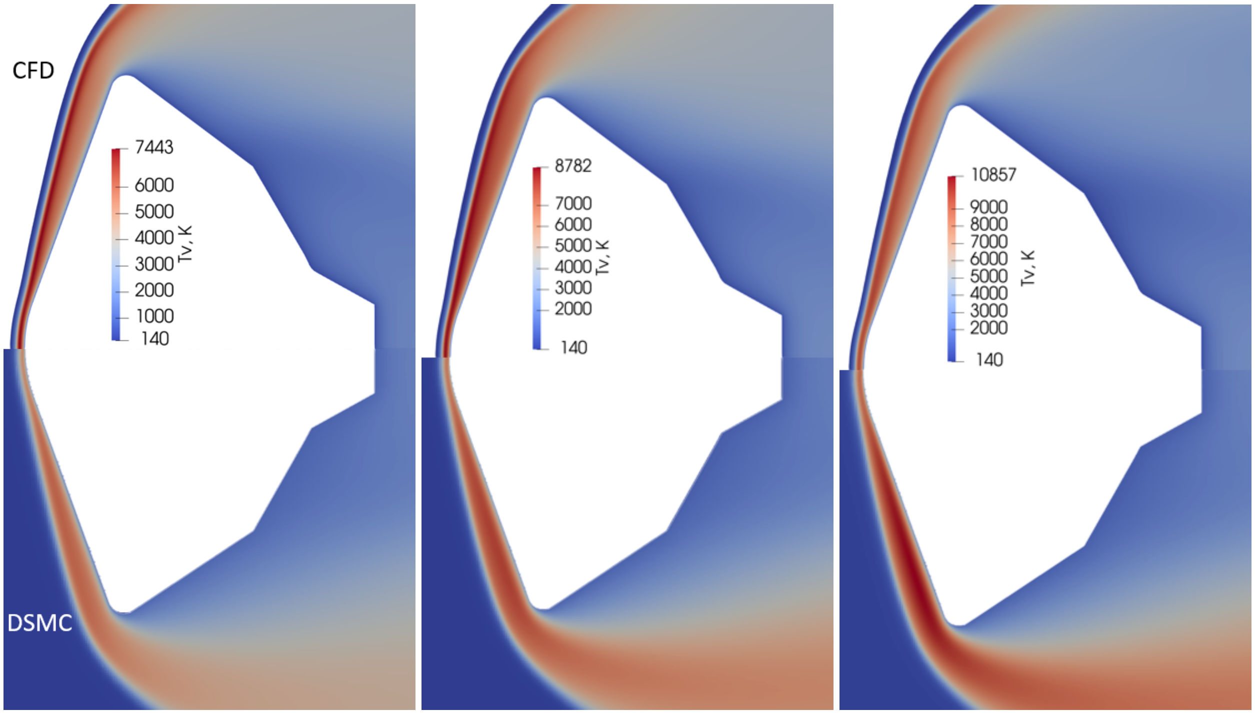

a) b) c)

Fig. 12 Vibrational temperature DPLR and SPARTA comparison at 80 km at Mars with a) 6 km/s, b) 7 km/s, and c) 8 km/s velocities.

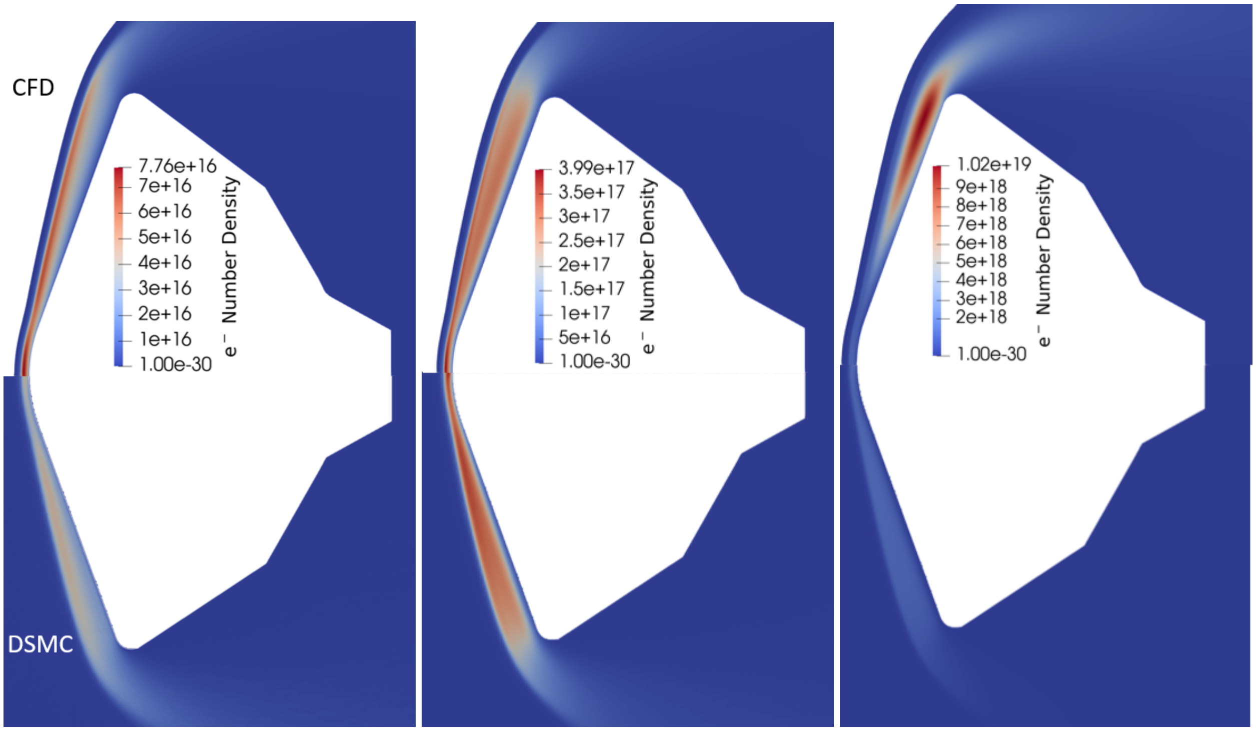

a) **b)** **c)**

Fig. 13 Electron number density CFD and DSMC comparison at 80 km at Mars with a) 6 km/s, b) 7 km/s, and c) 8 km/s velocities.

C. Aerodynamic and Heating Results

Because each CFD simulation is at 0° angle of attack, the lift and moment coefficients are 0. The drag coefficient for each CFD case is given in Table 1. The simulations assumed laminar flow with no turbulence model, so the turbulent regions behind the shoulder were not accurately solved. The unsteady flow behind the shoulder caused oscillations of the drag coefficient, and the values reported here are averages over many cycles. In general, the results agree well with Newtonian theory, which predicts a drag coefficient of 1.7.

Table 1 Drag Coefficient for 70° Spherecone in a Mars and Venus Atmosphere

	Freestream Velocity (m/s)							
Freestream Density (kg/m^3)	5.0	6.0	7.0	8.0	9.0	10.0	11.0	12.0
2.15e-6	1.69	1.69	1.68	1.69	1.70	1.71	1.71	1.72
2.84e-5	1.70	1.71	1.70	1.71	1.71	1.71	1.71	1.71
4.05e-4	1.71	1.71	1.71	1.71	1.71	1.71	1.71	1.71
3.21e-3	1.71	1.71	1.70	1.71	1.71	1.71	1.69	1.70

The surface heat rate predicted by DPLR is the convective heat rate with no magnetic field interaction. Radiative heat rate was not considered in the simulations. MHD is known to reduce heat transfer to the vehicle [65], so the heat rate values in this study are likely higher than the values with MHD. They are presented here for comparison with future studies. The maximum heat rate for each case is shown in Fig. 14.

D. Electrical Conductivity Results

The electrical conductivity is compared to several studies in literature. Because the electrical conductivity is highly dependent on the composition of the flow, only studies for the Martian atmosphere were considered for comparison. There are limited studies in literature that document electrical conductivity in a Martian or Venetian atmosphere, and there were no data available for a 70° spherecone geometry. As a result, none of the results in this study are expected to match literature exactly; however, the electrical conductivity should be on the same order of magnitude for the same freestream conditions, particularly near the stagnation region where the geometry is locally a sphere.

The electrical conductivity and ion species mole fractions for 60 km Mars altitude at 10 km/s was calculated in Fig. 4 of Fujino (2016) [1]. The ion species' mole fractions and electrical conductivity profile for the same freestream density and velocity is shown in Fig. 15. The mole fractions in Fig. 15a agree well with the literature [1]. The profiles follow the same trend, and the magnitude of each species is within an order of magnitude between the two cases. The shock width in this study is much smaller because MHD interactions were not accounted for in the flowfield in this study.

In general, the electrical conductivity profiles compare reasonably. The peak electrical conductivity is 1274 S/m while the maximum is approximately 1600 S/m in [1]. The conductivity decreases to 800 S/m in the shock along the frustum in both cases. The small difference in magnitude is likely due to the different geometries and possibly a difference in the electron collision frequency calculation, which is not explicitly stated in [1].

The second literature comparison for electrical conductivity is Fig. 8 in Moses et al. [6]. The study used a 6.5 m radius cylinder in 7 km/s flow with a density of 2×10^{-3} kg/m^3. Note that the electrical conductivity was calculated with a different method in [6] ($\sigma = 2.7 \times 10^5 \frac{n_e}{n}$ S/m). For a better comparison, the electrical conductivity for a case with similar freestream conditions in this study was calculated with the same method in Fig. 16a. The electrical conductivity was recalculated with Eq. 16 in Fig. 16b. The electrical conductivity magnitude agrees well in Fig. 16a when the same calculation method is used. The peak electrical conductivity is 161 S/m, which is just 6% lower than the 170 S/m in [6]. The conductivity in Fig. 16b is approximately double that of Fig. 16a, which indicates that the simplified conductivity model works reasonably well for this case. The temperature and ion density profiles are also provided in Fig. 16c and d. The magnitude of temperature agrees well with literature, but the 70° spherecone has a higher electron number density. Both the 70° spherecone and cylinder have a shock temperature of approximately 6000 K throughout. The 70° spherecone has an average electron number density of approximately 6.5×10^{14} cm^{-3} while the cylinder has an average electron density of approximately 5×10^{14} cm^{-3}.

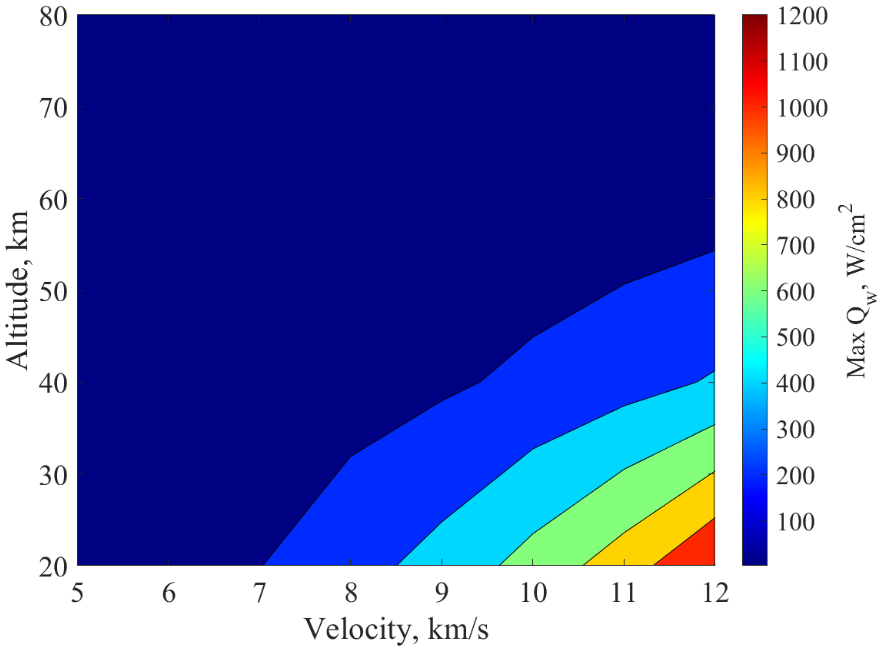

Fig. 14 Maximum convective heat rate for each CFD case.

Note that the ionization fraction $\frac{n_e}{n}$ should be less than 0.01 for the simplified model in [6] to be used. The maximum ionization fraction for each case is shown in Fig. 17. The ionization fraction is less than 0.01 when the velocity is 8 km/s or lower. Above 8 km/s, a significant portion of the particles are ionized, with a maximum ionization of 0.3145% at the highest velocity and lowest density. If the vehicle is going significantly faster than 12 km/s, such as for a Neptune or Uranus entry, MHD force calculations may need to account for ion movement due to a reentry plasma that is nearly completely ionized.

In general, the electrical conductivity magnitude near the stagnation line agrees with literature even if the vehicle geometry is different. It may be useful to understand how the electrical conductivity scales with altitude and velocity over a wider range of conditions than what is currently in literature. The stagnation line conductivity is compared for all 32 CFD cases in Fig. 19a-d. In all cases, the electrical conductivity magnitude is highly dependent on the velocity. The higher density cases have sharper rises across the shock (Fig. 19a) compared to the lower density cases (Fig. 19d). At a higher density, the shock is more well-defined and heats the flow more, resulting in more ionization.

Although the electrical conductivity can have large magnitudes for some cases, the Hall effect has been shown to significantly decrease the electric current density magnitude [24]. The electrical conductivity corrected for Hall and ion slip effects was calculated assuming the magnet configuration described in Section IV.C. The effective electrical conductivity, σ_{eff}, that is calculated with Eqs. (13) - (17) along the stagnation line is given for each case in Fig. 19a-d. At 20 km at Mars, there is a small decrease in the conductivity when the Hall and ion slip effects are accounted for, with a larger decrease at lower velocities. At 5 km/s, the effective electrical conductivity is approximately 4 times lower than

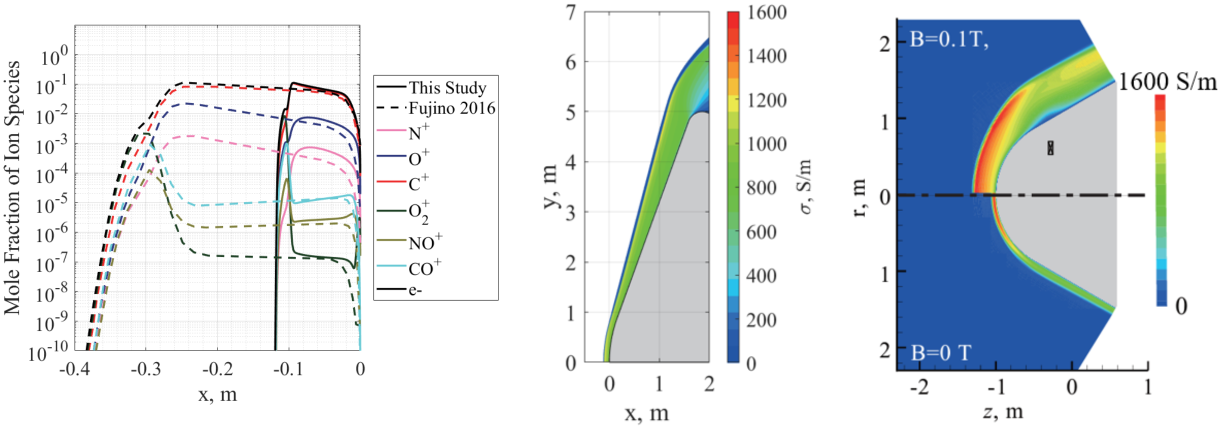

a)

b)

Fig. 15 Comparison of a) ion species mole fractions and b) electrical conductivity at 60 km Mars altitude, 10 km/s. The freestream conditions are similar to those in [1].*

the conductivity without accounting for Hall and ion slip effects. The Hall and ion slip effects are negligible at 12 km/s. At 80 km, the Hall effect dominates and causes the effective conductivity to be only 6% of the original value at 12 km/s. The Hall and ion slip effects significantly reduce the effective conductivity at low densities. The normalized Hall parameter Ω_e/B and ion slip parameter $\Omega_e\Omega_i/B^2$ for several cases are shown in Fig. 18. Figure 18a shows the two parameters along the stagnation line for $\rho = 2.15 \times 10^{-6}$ kg/m^3 for three different velocities: 12 km/s, 8 km/s, and 5 km/s. There is significant variation in both parameters in the shock layer. Near the shock, the Hall parameter takes a value of $10^4 - 10^6$ while the ion slip parameter takes a value of $10^5 - 10^7$. Close to the vehicle, both parameters have lower values of 10^4 or less. With the low density, both parameters are high. Figure 18b shows similar information at $\rho = 3.21 \times 10^{-3}$ kg/m^3. Both parameters are constant throughout the shock layer, and they are both significantly lower than 1 at high velocities. The low values indicate that Hall and ion slip effects can be neglected at high densities and high velocities.

The relative magnitude of electrical conductivity between each case is estimated by integrating over the volume $\left(\iiint \sigma dV\right)$. The integrated electrical conductivity for each case is shown in Table 2. In general, electrical conductivity increases as altitude decreases (higher density) and as velocity increases.

As expected, electrical conductivity always increases as velocity increases. At high velocities, there is enough energy to ionize a significant portion of the flow. Interestingly, at low velocities, higher conductivity is found at high altitudes while the maximum conductivity is found at lower altitudes for high velocities. The electrical conductivity, vibrational temperature, and translational temperature for the 5 km/s, 20 km case and the 5 km/s, 80 km case are compared in Fig. 20. In Fig. 20a, the high-density case, there is little variation in the shock layer for all three quantities because the high

---

*From Fujino, T. and Takahashi, T., "Numerical Simulation of Mars Entry Flight Using Magnetohydrodynamic Parachute Effect"; reprinted by permission of the American Institute of Aeronautics and Astronautics, Inc.

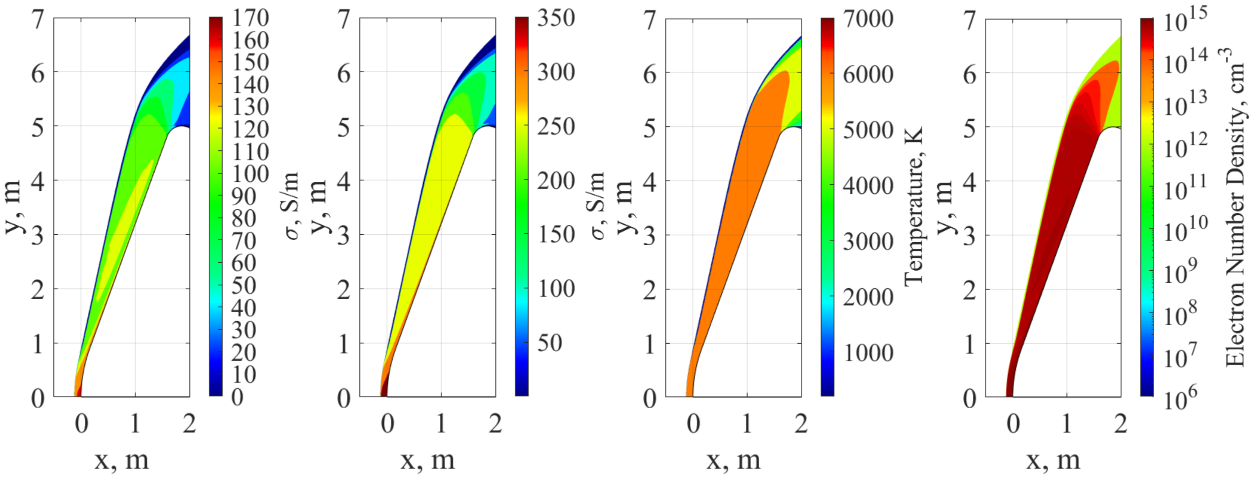

a) **b)** **c)** **d)**

Fig. 16 Comparison of a) simplified electrical conductivity model ($\sigma = 2.7 \times 10^5 \frac{n_e}{n}$ S/m) [6] and b) electrical conductivity from Eq. 16 for $\rho = 3.21 \times 10^{-3}$ kg/m^3, V = 7 km/s. The c) temperature and d) electron number density are given for comparison with Fig. 8 in [6].

collision frequency brings the system to equilibrium quickly. At high altitudes, there are fewer collisions, and it may take longer for flow that was initially ionized in the shock to recombine. In Fig. 20b, the electrical conductivity and temperatures are higher in the shock layer because there are too few collisions to reach thermal equilibrium quickly.

Table 2 Integrated Electrical Conductivity for Each CFD Condition Given in S/m

	Freestream Velocity (km/s)							
Freestream Density (kg/m^3)	5	6	7	8	9	10	11	12
2.15E-6	1.61E+02	1.21E+03	3.59E+05	1.92E+06	5.20E+06	6.83E+06	8.96E+06	1.15E+07
2.84E-05	5.55E+02	1.46E+03	7.96E+05	1.33E+06	1.78E+06	2.29E+06	3.39E+06	7.33E+06
4.05E-04	7.09E+03	1.52E+04	5.80E+05	1.11E+06	1.47E+06	2.02E+06	3.28E+06	6.41E+06
3.21E-03	6.34E+04	1.98E+05	6.75E+05	2.67E+06	3.15E+06	3.93E+06	4.58E+06	5.42E+06

E. Magnetohydrodynamic Force

Since the CFD simulations did not include magnetic field interactions in the flow, the method of calculating MHD force in this study is compared to literature that did include magnetic field interactions. The magnet in Section IV.C is the dipole magnet configuration from Ref. [23]. The magnet configuration was used to calculate the MHD force under the two conditions denoted in Table 3. To estimate the force at the desired condition, the force is calculated at each CFD condition, and 2-dimensional interpolation is done. Note that the MHD force is not expected to be identical due to a difference in geometry. Reference [23] used a 45° spherecone, which causes the shock layer to have a larger magnetic field strength near the nose. A 70° spherecone was used in this study. The goal of the force calculation presented in

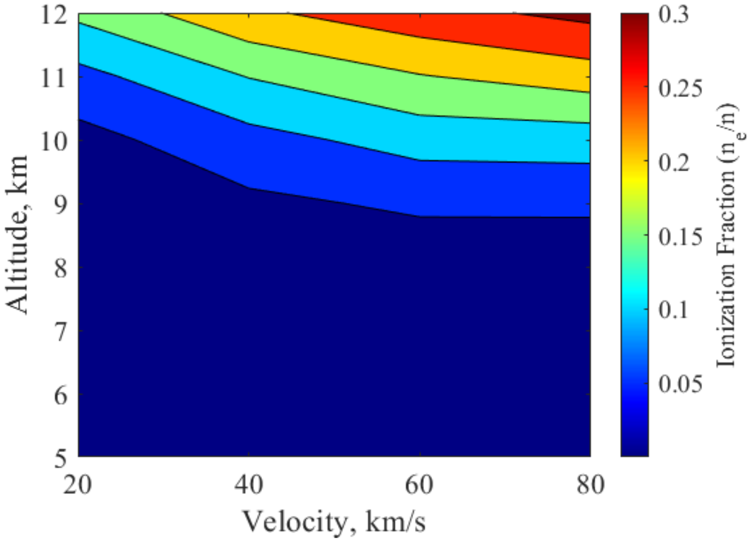

Fig. 17 Maximum ionization fraction in the flowfield for each freestream condition.

Table 3 Freestream Conditions For Literature Comparison [23]

Altitude	Velocity	Tabuchi 2023 MHD Force [23]	MHD Force in Current Study
40 km	7.667 km/s	5 kN	1.47 kN
50 km	7.942 km/s	5 kN	0.88 kN

this paper is to provide a first-order estimate of the force, so an MHD fore that is within an order of magnitude of the literature is acceptable.

At 40 km, the MHD force is estimated to be 1.47 kN, and at 50 km it is 0.88 kN. In the literature, the force is approximately 5 kN for each case [23]. Although the values are not identical, the approximation can still get a solution of the same order of magnitude as one that solves Ohm's law at a fraction of the computational cost. The majority of the difference in force is likely due to the difference in geometry.

The MHD force was calculated for each CFD condition assuming the magnet configuration described in Section IV.C. The force for each velocity and density is given in Appendix B. The force at Mars from 16 of the CFD conditions is given in Fig. 21. The magnet is axisymmetric, so the force is in the drag direction. The four trajectories discussed in Section III are co-plotted on the force. Note that the trajectories do not include the MHD force in the equations of motion; the plot only shows the maximum possible MHD force if a vehicle did fly the trajectories with the magnet configuration described in Section IV.C. The maximum force experienced by any of the three trajectories is approximately 0.1 kN; for the majority of the trajectories it is significantly lower. A 0.1 kN force is not strong enough to have any meaningful impact on the trajectory regardless of mission size. While MHD could have energy storage or communication applications at Mars, it is not an effective control mechanism without a method of artificially increasing the electrical conductivity.

The MHD force at Venus is given in Fig. 22a. The two aerocapture trajectories are co-plotted over the force. The

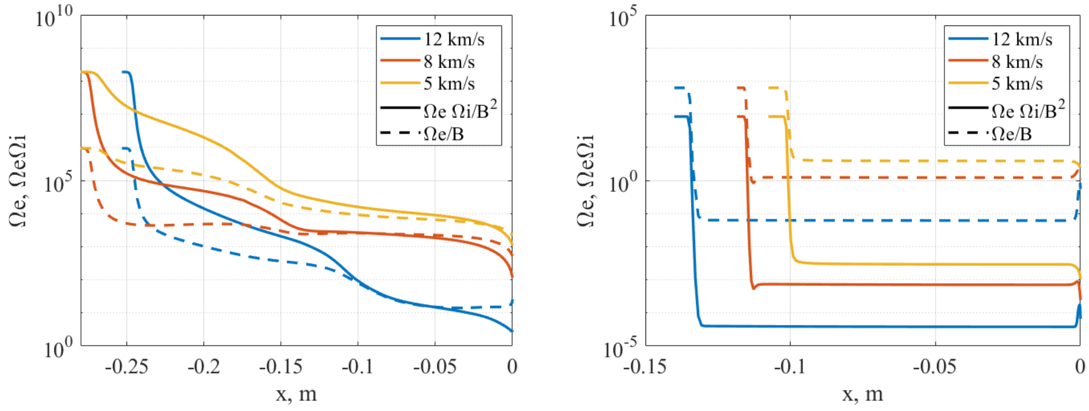

a) **b)**

Fig. 18 Hall parameter on the stagnation line for 12 km/s, 8 km/s, and 5 km/s for a) ρ = 2.15 × 10^{-6} kg/m^3 and b) ρ = 3.21 × 10^{-3} kg/m^3.

force at Venus is significantly higher than at Mars due to the higher velocities. Both trajectories have a maximum MHD force of approximately 10 kN. The ratio of MHD force to aerodynamic force is given in Fig. 22b. Early in the trajectory, MHD force exceeds the aerodynamic force. At a minimum, the MHD force magnitude is approximately 40% the drag force magnitude. The control authority at Venus is significant, and it could be used as a control mechanism for Venus aerocapture or aerogravity assist missions.

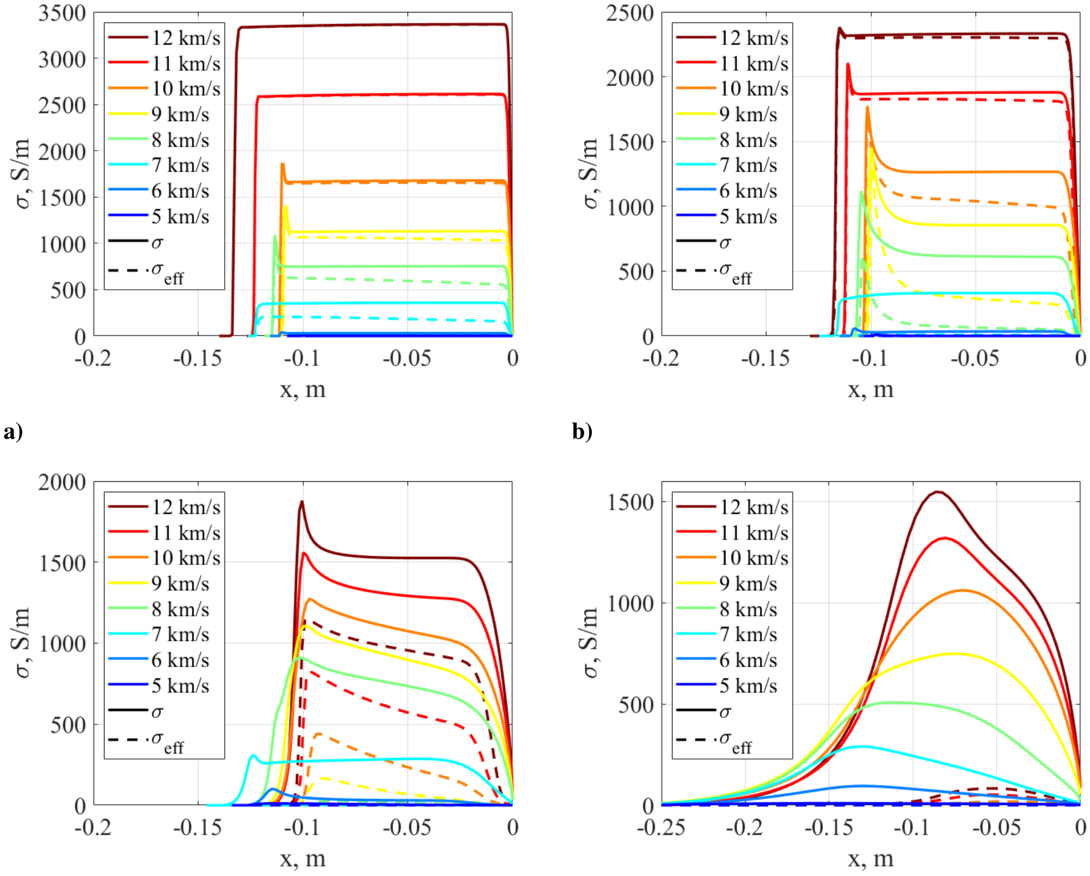

a)

b)

c)

d)

Fig. 19 Electrical conductivity along the stagnation line for velocities between 5 - 12 km/s for a) ρ = 3.12 × 10^{-3} kg/m^3 (20 km Mars), b) ρ = 4.05 × 10^{-4} kg/m^3 (40 km Mars), c) ρ = 2.84 × 10^{-5} kg/m^3 (60 km Mars), and d) ρ = 2.15 × 10^{-6} kg/m^3 (80 km Mars).

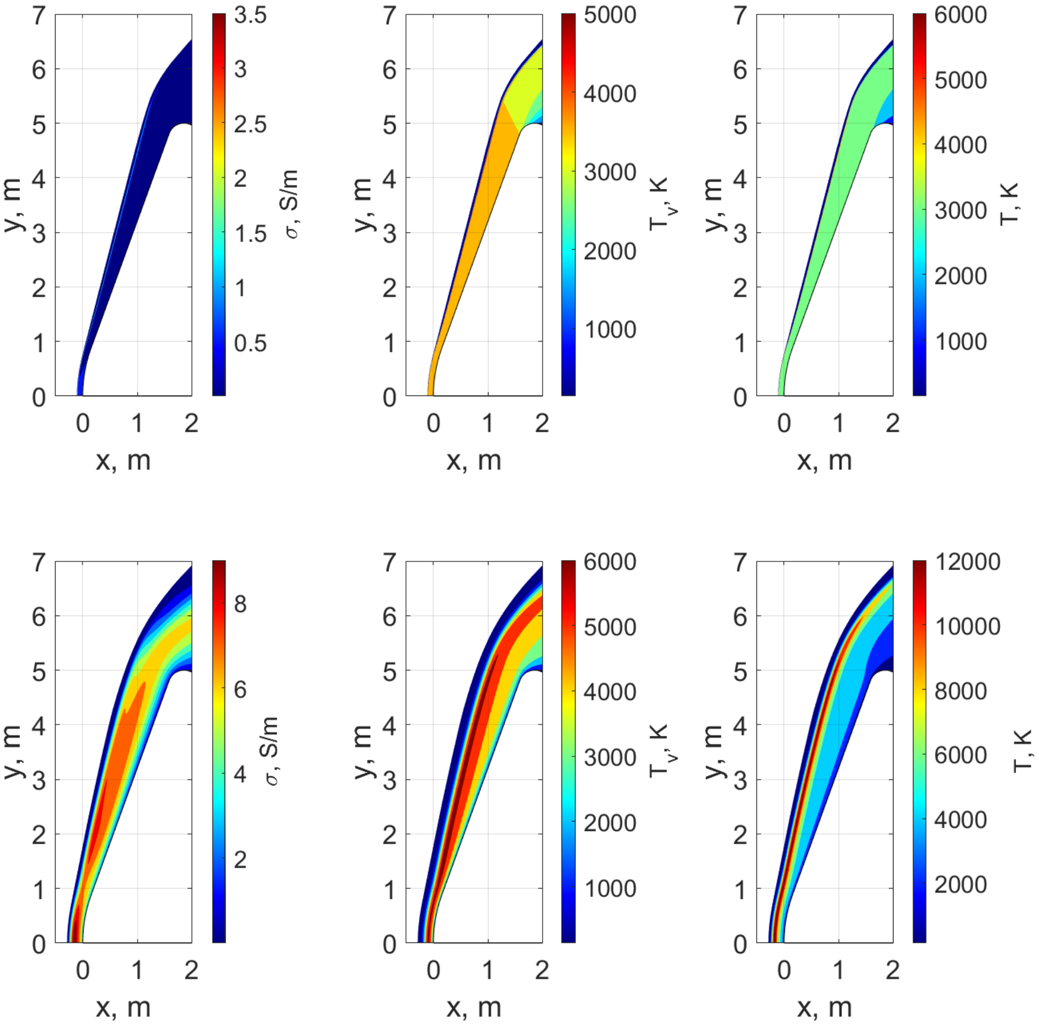

a)

b)

Fig. 20 Comparison of electrical conductivity, vibrational temperature, and translational temperature for the a) 20 km (high density) case and b) 80 km (low density) case.

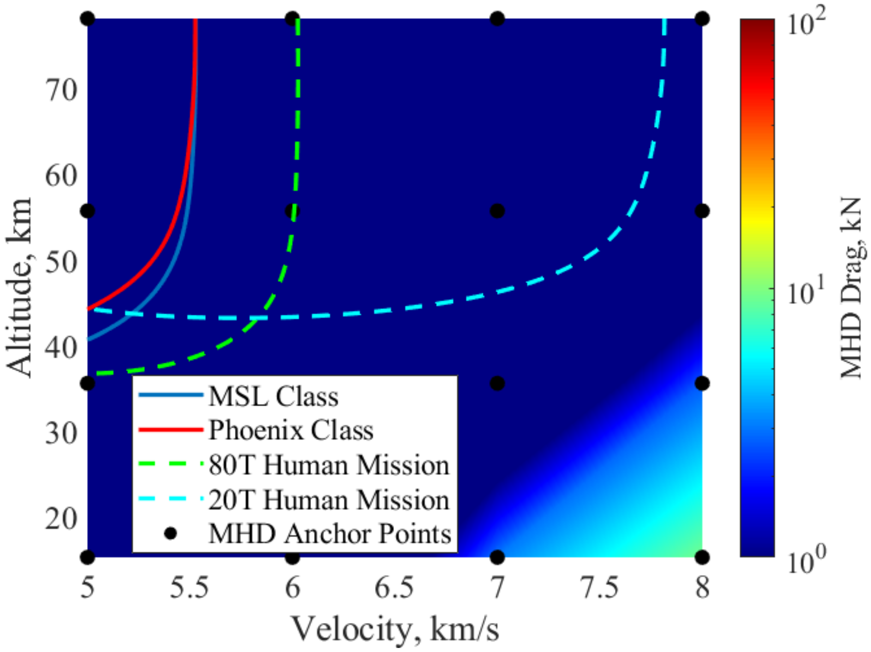

Fig. 21 MHD force computed from CFD results for each flight condition at Mars.

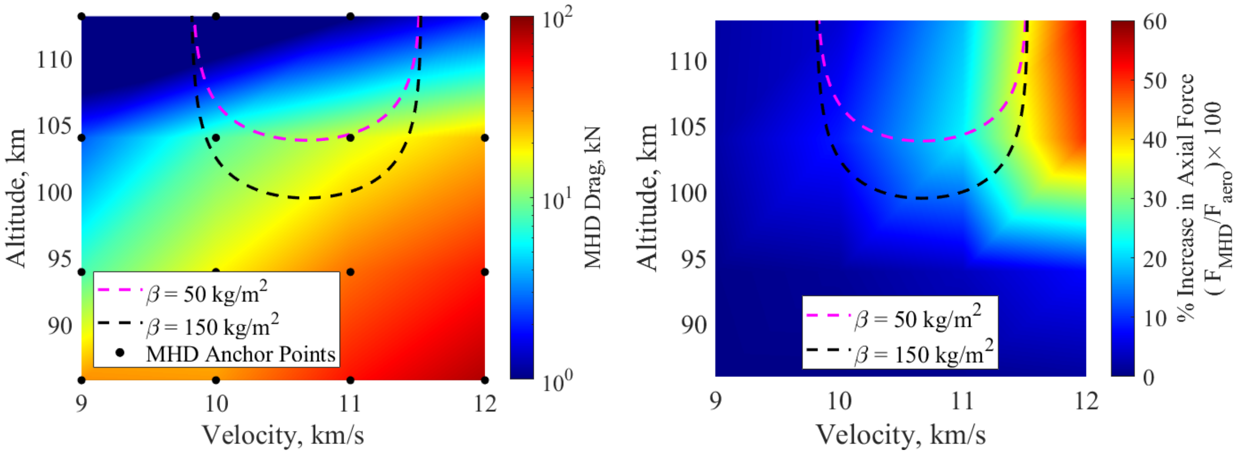

a)

b)

Fig. 22 CFD results at each flight condition are used to calculate a) the total magnitude of the MHD force and b) the percent increase in aerodynamic drag at Venus.

VI. Conclusions

Thirty-two freestream conditions were selected to create an electrical conductivity database. The Navier-Stokes equations were solved to determine the temperature, shock volume, velocity, and number density of each species over the flowfield. The temperature and number densities were used to calculate the electrical conductivity field at each condition. By integrating the electrical conductivity over the volume, it was determined that the electrical conductivity always increases as velocity increases. At low velocities, the electrical conductivity is higher at high altitudes because there are fewer collisions to allow electrons to recombine with parent ions. The electrical conductivity is higher at low altitudes with high velocities because the temperature is high enough to ionize the flow, and higher density leads to faster equilibrium.

Three of the 80 km computational fluid dynamics solutions were compared against similar Direct Simulation Monte Carlo simulations from a previous study and show reasonable agreement. In general, Direct Simulation Monte Carlo predicts thicker shocks and lower electron number density. The vibrational temperatures agree well between the two softwares.

A comparison with literature indicates that a decoupled approach of calculating the MHD force that was used in this study can get accuracy within an order of magnitude for less cost. The force calculation method in this paper also provides more flexibility in calculating the force for different magnetic fields.

Finally, the MHD force was calculated at both Mars and Venus assuming a single powerful magnet located on the vehicle's central axis 2m behind the forebody. Results indicate that there is not sufficient control authority to use MHD as a control mechanism at Mars without artificially increasing the electrical conductivity of the flow, but there may be sufficient control authority for a drag-modulated aerocapture at Venus, which has higher entry velocities.

Future trajectory studies may utilize the electrical conductivity results for any magnet configuration using the force model presented in this paper. The electrical conductivity for a 10 m diameter 70 deg spherecone can be interpolated from the given dataset for a freestream velocity between 6-12 km/s and freestream density between $2.15 \times 10^{-6} - 3.21 \times 10^{-3}$ kg/m^3.

Appendix A - Chemical Reactions

Table 4 Arrhenius Constants for Chemical Reactions

			k_f	
Reaction Number	Reaction	A	r	θ, K
	Dissociation			
1	$CO_2 + X \rightarrow CO + O + X$	See Table 5	-1.50	6.328×10^4
2	$CO + X \rightarrow C + O + X$	See Table 5	-1.00	1.290×10^5
3	$N_2 + X \rightarrow N + N + X$	See Table 5	-1.60	1.132×10^5
4	$O_2 + X \rightarrow O + O + X$	See Table 5	-1.50	5.936×10^4
5	$NO + X \rightarrow N + O + X$	See Table 5	0.00	7.550×10^4
6	$C_2 + X \rightarrow C + C + X$	See Table 5	-1.00	7.150×10^4
7	$CN + X \rightarrow C + N + X$	See Table 5	-0.40	7.100×10^4
	Exchange			
8	$CO_2 + O \rightarrow O_2 + CO$	2.71×10^{11}	0.00	3.380×10^4
9	$CO + C \rightarrow C_2 + O$	2.40×10^{14}	-1.00	5.800×10^4
10	$CO + N \rightarrow CN + O$	1.00×10^{11}	0.00	3.860×10^4
11	$CO + NO \rightarrow CO_2 + N$	3.00×10^{03}	0.88	1.330×10^4
12	$CO + O \rightarrow O_2 + C$	3.90×10^{10}	-0.18	6.920×10^4
13	$C_2 + N_2 \rightarrow CN + CN$	1.50×10^{10}	0.00	2.100×10^4
14	$CN + C \rightarrow C_2 + N$	3.00×10^{11}	0.00	1.810×10^4
15	$CN + O \rightarrow NO + C$	1.60×10^{09}	0.10	1.460×10^4
16	$CO + N \rightarrow NO + C$	1.10×10^{11}	0.07	5.350×10^4
17	$N_2 + C \rightarrow CN + N$	1.10×10^{11}	-0.11	2.320×10^4
18	$N_2 + CO \rightarrow CN + NO$	1.20×10^{13}	-1.23	7.700×10^4
19	$N_2 + O \rightarrow NO + N$	6.00×10^{10}	0.10	3.800×10^4
20	$O_2 + N \rightarrow NO + O$	2.49×10^{06}	1.18	4.010×10^3

Table 4 Arrhenius Constants for Chemical Reactions

		k_f		
Reaction Number	Reaction	A	r	θ, K
	Electron-impact Dissociation			
21	$C + e \rightarrow C^+ + e + e$	3.70×10^{28}	-3.00	1.307×10^5
22	$N + e \rightarrow N^+ + e + e$	2.50×10^{31}	-3.82	1.686×10^5
23	$O + e \rightarrow O^+ + e + e$	3.90×10^{30}	-3.78	1.585×10^5
24	$CO + e \rightarrow CO^+ + e + e$	4.50×10^{11}	0.28	1.635×10^5
25	$O_2 + e \rightarrow O_2^+ + e + e$	2.19×10^7	1.16	1.300×10^5
	Ionized Exchange			
26	$CO + C^+ \rightarrow C + CO^+$	1.10×10^{10}	0.00	3.140×10^4
27	$NO^+ + C \rightarrow NO + C^+$	1.30×10^{10}	0.00	2.320×10^4
28	$NO^+ + N \rightarrow N_2 + O^+$	3.40×10^{10}	-1.08	1.280×10^4
29	$NO^+ + O \rightarrow N + O_2^+$	7.20×10^9	0.29	4.860×10^4
30	$NO^+ + O_2 \rightarrow NO + O_2^+$	2.40×10^{10}	0.41	3.260×10^4
31	$O_2 + C^+ \rightarrow C + O_2^+$	1.00×10^{10}	0.00	9.400×10^3
32	$O_2^+ + O \rightarrow O_2 + O^+$	2.19×10^7	1.16	1.300×10^5
	Ionization			
33	$C + O \rightarrow CO^+ + e$	8.80×10^5	1.00	3.310×10^4
34	$N + O \rightarrow NO^+ + e$	5.30×10^9	0.00	3.190×10^4
35	$O + O \rightarrow O_2^+ + e$	7.10×10^{-1}	2.70	8.060×10^4

Table 5 Arrhenius Coefficient A for Dissociation Reactions

	Reaction Number						
	1	2	3	4	5	6	7
$X = CO_2$	1.4e+19	3.0e+18	7.0e+18	2.0e+18	1.1e+14	4.5e+15	6.0e+12
$X = CO$	1.4e+19	3.0e+18	7.0e+18	2.0e+18	5.0e+12	4.5e+15	6.0e+12
$X = CO^+$	1.4e+19	3.0e+18	7.0e+18	2.0e+18	5.0e+12	4.5e+15	6.0e+12
$X = C_2$	1.4e+19	3.0e+18	7.0e+18	2.0e+18	5.0e+12	4.5e+15	6.0e+12
$X = N_2$	1.4e+19	3.0e+18	7.0e+18	2.0e+18	5.0e+12	4.5e+15	6.0e+12
$X = O_2$	1.4e+19	3.0e+18	7.0e+18	2.0e+18	5.0e+12	4.5e+15	6.0e+12
$X = O_2^+$	1.4e+19	3.0e+18	7.0e+18	2.0e+18	5.0e+12	4.5e+15	6.0e+12
$X = NO$	1.4e+19	3.0e+18	7.0e+18	2.0e+18	1.1e+14	4.5e+15	6.0e+12
$X = NO^+$	1.4e+19	3.0e+18	7.0e+18	2.0e+18	5.0e+12	4.5e+15	6.0e+12
$X = CN$	1.4e+19	3.0e+18	7.0e+18	2.0e+18	5.0e+12	4.5e+15	6.0e+12
$X = C$	2.8e+19	3.0e+18	3.0e+19	1.0e+19	1.1e+14	4.5e+15	6.0e+12
$X = C^+$	1.4e+19	3.0e+18	7.0e+18	2.0e+18	5.0e+12	4.5e+15	6.0e+12
$X = N$	2.8e+19	3.0e+18	3.0e+19	1.0e+19	1.1e+14	4.5e+15	6.0e+12
$X = N^+$	1.4e+19	3.0e+18	7.0e+18	2.0e+18	5.0e+12	4.5e+15	6.0e+12
$X = O$	2.8e+19	3.0e+18	3.0e+19	1.0e+19	1.1e+14	4.5e+15	6.0e+12
$X = O^+$	1.4e+19	3.0e+18	7.0e+18	2.0e+18	5.0e+12	4.5e+15	6.0e+12
$X = e^-$	0.0e+0	0.0e+0	0.0e+0	0.0e+0	0.0e+0	0.0e+0	0.0e+0

Appendix B - MHD Force Table for a Single Magnet Scaled to 0.5 T at Stagnation Point

Table 6 MHD Force in kN for Single Dipole Magnet Located at x=0.875 m Scaled to 0.5T at Stagnation Point

	Freestream Velocity (km/s)							
Freestream Density (kg/m^3)	5	6	7	8	9	10	11	12
2.15e-6	2.2e-5	2.5e-4	1.5e-3	8.1e-2	1.8e-1	3.3e-1	9.5e-1	1.9e+0
2.84E-05	5.9e-5	3.5e-4	3.0e-2	2.4e-1	2.7e+0	8.1e+0	1.5e+1	2.4e+1
4.05E-04	1.1e-4	1.9e-3	2.3e-1	2.6e+0	7.7e+0	1.8e+1	3.4e+1	5.1e+1
3.21E-03	2.3e-3	1.0e-1	3.1e+0	9.4e+0	2.9e+1	2.8e+1	5.3e+1	8.0e+1

VII. Acknowledgments

This work was supported by a NASA Space Technology Graduate Research Opportunity. Resources supporting this work were provided by the NASA High-End Computing (HEC) Program through the NASA Advanced Supercomputing (NAS) Division at Ames Research Center.

References

[1] Fujino, T., and Takahashi, T., "Numerical Simulation of Mars Entry Flight Using Magnetohydrodynamic Parachute Effect," 47th AIAA Plasmadynamics and Lasers Conference, AIAA, 2016-3227. doi:10.2514/6.2016-3227.

[2] Kranc, S, Yuen, M.C., and Cambel, A.B., "Experimental Investigation of Magnetoaerodynamic Flow Around Blunt Bodies," NASA Contractor Reports, 1969. doi:10.2514/6.1967-729.

[3] Kawamura, M., Matsuda, A., Katsurayama, H., Otsu, H., Konigorski, D., Sato, S., and Abe, T., "Experimental Study on Drag Enhancement in Electrodynamic Heat Shield for a Blunt Body in a Weakly Ionized Plasma Flow," 38th AIAA Plasmadynamics and Lasers Conference, Vol. 1, AIAA, 2007-3889, pp. 175–186. doi:10.2514/6.2007-3889.

[4] Ali, H. K., and Braun, R. D., "Modeling Magnetohydrodynamic Energy Generation and Storage in Planetary Entry System Conceptual Design," Journal of Spacecraft and Rockets, Vol. 55, No. 2, 2018, pp. 356–364. doi:10.2514/1.A33948.

[5] Ali, H. K., and Braun, R. D., "Application of Magnetohydrodynamic Energy Generation to Planetary Entry Vehicles," 12th International Energy Conversion Engineering Conference, AIAA, 2014-3556. doi:10.2514/6.2014-3556.

[6] Macheret, S. O., Shneider, M. N., Candler, G. V., Moses, R. W., and Kline, J. F., "Magnetohydrodynamic Power Generation for Planetary Entry Vehicles," 35th AIAA Plasmadynamics and Lasers Conference, AIAA, 2004-2560. doi:10.2514/6.2004-2560.

[7] Moses, R. W., "Plasma Assisted ISRU at Mars," 15th International Conference on MHD Energy Conversion, Vol. 2, 2005, pp. 468–477.

[8] Moses, R. W., "Regenerative Aerobraking," AIP Conference Proceedings, Vol. 746, 2005, pp. 1361–1370. doi:10.1063/1.1867266.

[9] Bityurin, V., and Bocharov, A., "On Efficiency of Heat Flux Mitigation by the Magnetic Field in MHD Re-entry Flow," 42nd AIAA Plasmadynamics and Lasers Conference in conjunction with the 18th International Conference on MHD Energy Conversion (ICMHD), 2011, p. 3463. doi:10.2514/6.2011-3463.

[10] Müller, R. A., Pagan, A. S., Upadhyay, P. P., and Herdrich, G., "Numerical Assessment of Magnetohydrodynamic Heat Flux Mitigation for Pico-sized Entry Capsule Mockup," Journal of Thermophysics and Heat Transfer, Vol. 33, No. 4, 2019, pp. 1018–1025. doi:10.2514/1.T5679.

[11] Kim, M., and Boyd, I. D., "Effectiveness of a Magnetohydrodynamics System for Mars Entry," Journal of Spacecraft and Rockets, Vol. 49, No. 6, 2012, pp. 1141–1149. doi:10.2514/1.A32256.

[12] Kim, M., and Gülhan, A., “Plasma Manipulation Using a MHD-based Device for a Communication Blackout in Hypersonic Flights,” Proceedings of 5th International Conference on Recent Advances in Space Technologies-RAST2011, IEEE, 2011, pp. 412–417. doi:10.1109/RAST.2011.5966868.

[13] Ali, H. K., and Braun, R. D., “Effects of Magnetohydrodynamic Energy Generation on Planetary Entry Vehicle Flight Dynamics,” 13th International Energy Conversion Engineering Conference, AIAA, 2015-4179. doi:10.2514/6.2015-4179.

[14] van Oeveren, S. B., and Gildfind, D., “Optimised Magnetic Field Strengths for Venus Atmospheric Entry using Magnetohydrodynamic Aerobraking,” AIAA SCITECH 2023 Forum, 2023, p. 2562. doi:10.2514/6.2023-2562.

[15] Smith, D. R., Chia, Y. S., and Gildfind, D., “Heat Transfer Mitigation Along Superorbital Reentry Trajectories Using Magnetohydrodynamic Aerobraking,” AIAA Aviation 2022 Forum, 2022, p. 3649. doi:10.2514/6.2022-3649.

[16] CAMBEL, A. B., and PORTER, R. W., “Hall Effect in Flight Magnetogasdynamics.” AIAA Journal, Vol. 5, No. 12, 1967, pp. 2208–2213. doi:10.2514/3.4410.

[17] Ogilvie, J. C., Gildfind, D., Gollan, R., and Gibbons, N. N., “Feasibility of MHD Aerobraking for Use in Martian Atmospheric Entry,” AIAA SCITECH 2023 Forum, 2023, p. 2560. doi:10.2514/6.2023-2560.

[18] Ying, Y., Zhe Feng, Y., and Weizhong, D., “Blackout Mitigation by External Electromagnetic Field in Re-entry Vehicles,” 2019 IEEE International Conference on Computational Electromagnetics, Institute of Electrical and Electronics Engineers Inc., 2019. doi:10.1109/COMPEM.2019.8778957.

[19] Bityurin, V. A., Bocharov, A. N., and Popov, N. A., “Numerical Simulations on MHD Break in Hypersonic Flow,” Journal of Physics: Conference Series, Vol. 1394, Institute of Physics Publishing, 2019. doi:10.1088/1742-6596/1394/1/012019.

[20] Bityurin, V., Bocharov, A., and Lineberry, J., “Study of MHD Interaction in Hypersonic Flows,” 15th International Conference on MHD Energy Conversion and 6th Workshop on Magnetoplasma Aerodynamics, Moscow, 24-27 May, 2005, p. 399.

[21] Fujino, T., Yoshino, T., and Ishikawa, M., “Numerical Analysis of Reentry Trajectory Coupled with Magnetohydrodynamics Flow Control,” Journal of Spacecraft and Rockets, Vol. 45, No. 5, 2008, pp. 911–920. doi:10.2514/1.33385.

[22] Fujino, T., Sugita, H., Mizuno, M., Funaki, I., and Ishikawa, M., “Influences of Electrical Conductivity of Wall on Magnetohydrodynamic Control of Aeroynamic Heating,” Journal of Spacecraft and Rockets, Vol. 43, No. 1, 2006, pp. 63–70. doi:10.2514/1.13770.

[23] Tabuchi, K., Sumitomo, R., Tanaka, K., and Fujino, T., “Numerical Analysis of Magnetohydrodynamic Flow Control in Mars Direct and Orbital Entries,” AIAA SCITECH 2023 Forum, 2023, p. 2559. doi:10.2514/6.2023-2559.

[24] Fujino, T., Funaki, I., Mizuno, M., Sugita, H., and Ishikawa, M., “Numerical Studies of Influences of Hall Effect on MHD Flow Control Around Blunt Body OREX,” 35th AIAA Plasmadynamics and Lasers Conference, 2004, p. 2561. doi:10.2514/6.2004-2561.

[25] Fawley, D. M., Putnam, Z. R., D'Souza, S., and Borner, A., "Assessment of Electrical Conductivity in Rarefied Flow about Mars Entry Vehicles," AIAA SCITECH 2022 Forum, 2022, p. 0825. doi:10.2514/6.2022-0825.

[26] Way, D. W., Powell, R. W., Chen, A., Steltzner, A. D., San Martin, A. M., Burkhart, P. D., and Mendeck, G. F., "Mars Science Laboratory: Entry, Descent, and Landing System Performance," 2007 IEEE Aerospace Conference, IEEE, 2007, pp. 1–19. doi:10.1109/AERO.2007.352821.

[27] Braun, R. D., Wells, G. W., Lafleur, J. W., Verges, A. A., and Tiller, C. W., "Entry, Descent and Landing Challenges of Human Mars Exploration," Advances in the Astronautical Sciences, Vol. 125, 2006, pp. 325–340.

[28] Ilin, A. V., Cassady, L. D., Glover, T. W., and Chang Diaz, F. R., "VASIMR® Human Mission to Mars," Space, Propulsion & Energy Sciences International Forum, 2011, pp. 1–12.

[29] Wooster, P. D., Braun, R. D., Ahn, J., and Putnam, Z. R., "Mission Design Options for Human Mars Missions," The International Journal of Mars Science and Exploration, Vol. 3, 2007, pp. 12–28. doi:10.1555/mars.2007.0002.

[30] Dwyer-Cianciolo, A. M., Davis, J. L., Komar, D. R., Munk, M. M., Samareh, J. A., Powell, R. W., Shidner, J. D., Stanley, D. O., Wilhite, A. W., Kinney, D. J., et al., "Entry, Descent and Landing Systems Analysis Study: Phase 1 Report," Tech. rep., 2010.

[31] Christian, J. A., Wells, G., Lafleur, J. M., Verges, A., and Braun, R. D., "Extension of Traditional Entry, Descent, and Landing Technologies for Human Mars Exploration," Journal of spacecraft and rockets, Vol. 45, No. 1, 2008, pp. 130–141. doi:10.2514/1.31929.

[32] Dwyer-Cianciolo, A. M., and Polsgrove, T., "Human Mars Entry, Descent, and Landing Architecture Study: Phase 2 Summary," 2018 AIAA SPACE and Astronautics Forum and Exposition, 2018, p. 5190. doi:10.2514/6.2018-5190.

[33] Hofstetter, W., Wooster, P., Nadir, W., and Crawley, E., "Affordable Human Moon and Mars Exploration Through Hardware Commonality," Space 2005, 2005, p. 6757. doi:10.2514/6.2005-6757.

[34] Lyne, J. E., "Physiologically Constrained Aerocapture for Manned Mars Missions," No. NASA-TM-103954, 1992.

[35] Man-Systems Integration Standards, Rev. B, NASA STD-3000, July 1995.

[36] Craig, S., and Lyne, J. E., "Parametric Study of Aerocapture for Missions to Venus," Journal of spacecraft and rockets, Vol. 42, No. 6, 2005, pp. 1035–1038. doi:10.2514/1.2589.

[37] Dutta, S., Smith, B., Prabhu, D., and Venkatapathy, E., "Mission Sizing and Trade Studies for Low Ballistic Coefficient Entry Systems to Venus," 2012 IEEE Aerospace Conference, IEEE, 2012, pp. 1–14. doi:10.1109/AERO.2012.6187002.

[38] Schoenenberger, M., Norman, J. V., Karlgaard, C., Kutty, P., and Way, D., "Assessment of the Reconstructed Aerodynamics of the Mars Science Laboratory Entry Vehicle," Journal of Spacecraft and Rockets, Vol. 51, No. 4, 2014, pp. 1076–1093. doi:10.2514/1.A32794.

[39] Wright, M. J., White, T., and Mangini, N., Data Parallel Line Relaxation (DPLR) Code User Manual: Big Bend - Version 4.03.1, National Aeronautics and Space Administration, Ames Research Center, 2019.

[40] Johnston, C., Brandis, A., and Sutton, K., "Shock Layer Radiation Modeling and Uncertainty for Mars Entry," 43rd AIAA Thermophysics Conference, 2012, p. 2866. doi:10.2514/6.2012-2866.

[41] Candler, G., "The computation of weakly ionized hypersonic flows in thermo-chemical nonequilibrium [dissertation]," , 1998.

[42] Gurvich, L. V., and Veyts, I., Thermodynamic Properties of Individual Substances: Elements and Compounds, Vol. 2, CRC press, 1990.

[43] Kramida, A., Ralchenko, Y., Reader, J., and NIST ASD Team, "NIST Atomic Spectra Database (version 5.9)," [Online]. National Institute of Standards and Technology, Gaithersburg, MD, 2021. doi:10.6028/nist.fips.140-2, URL `https://www.nist.gov/pml/atomic-spectra-database`.

[44] Gupta, R. N., Yos, J. M., Thompson, R. A., and Lee, K.-P., "A Review of Reaction Rates and Thermodynamic and Transport Properties for an 11-species Air Model for Chemical and Thermal Nonequilibrium Calculations to 30000 K," 1990.

[45] Cubley, S. J., and Mason, E., "Atom-molecule and Molecule-molecule Potentials and Transport Collision Integrals for High-temperature Air Species," The Physics of Fluids, Vol. 18, No. 9, 1975, pp. 1109–1111.

[46] Stallcop, J. R., Partridge, H., Pradhan, A., and Levin, E., "Potential Energies and Collision Integrals for Interactions of Carbon and Nitrogen Atoms," Journal of thermophysics and heat transfer, Vol. 14, No. 4, 2000, pp. 480–488. doi:10.2514/2.6570.

[47] Stallcop, J. R., Partridge, H., and Levin, E., "Resonance Charge Transfer, Transport Cross Sections, and Collision Integrals for N+ (3 P)–N (4 S 0) and O+ (4 S 0)–O (3 P) Interactions," The Journal of Chemical Physics, Vol. 95, No. 9, 1991, pp. 6429–6439. doi:10.1063/1.461563.

[48] Stallcop, J. R., Partridge, H., and Levin, E., "Effective Potential Energies and Transport Cross Sections for Atom-molecule Interactions of Nitrogen and Oxygen," Physical Review A, Vol. 64, No. 4, 2001, p. 042722. doi:10.1103/PhysRevA.64.042722.

[49] Stallcop, J. R., Partridge, H., and Levin, E., "Effective Potential Energies and Transport Cross Sections for Interactions of Hydrogen and Nitrogen," Physical Review A, Vol. 62, No. 6, 2000, p. 062709. doi:10.1103/physreva.62.062709.

[50] Partridge, H., Stallcop, J. R., and Levin, E., "Transport Cross Sections and Collision Integrals for N (4So)-O+ (4So) and N+ (3P)-O (3P) Interactions," Chemical physics letters, Vol. 184, No. 5-6, 1991, pp. 505–512. doi:10.1016/0009-2614(91)80026-t.

[51] Levin, E., Partridge, H., and Stallcop, J. R., "Collision Integrals and High Temperature Transport Properties for NN, OO, and NO," Journal of Thermophysics and Heat Transfer, Vol. 4, No. 4, 1990, pp. 469–477. doi:10.2514/3.210.

[52] Murphy, A. B., "Transport Coefficients of Air, Argon-air, Nitrogen-air, and Oxygen-air Plasmas," Plasma Chemistry and Plasma Processing, Vol. 15, No. 2, 1995, pp. 279–307. doi:10.1007/bf01459700.

[53] Riabov, V. V., “Approximate Calculation of Transport Coefficients of Earth and Mars Atmospheric Dissociating Gases,” Journal of Thermophysics and Heat Transfer, Vol. 10, No. 2, 1996, pp. 209–216. doi:10.2514/3.777.

[54] Ryabov, V., “Transfer Coefficient of Multicomponent Air with Sublimation Products of Graphite,” Journal of Engineering Physics, Vol. 55, No. 1, 1988, pp. 786–791. doi:10.1007/bf00878126.

[55] Bzowski, J., Kestin, J., Mason, E., and Uribe, F., “Equilibrium and Transport Properties of Gas Mixtures at Low Density: Eleven Polyatomic Gases and Five Noble Gases,” Journal of physical and chemical reference data, Vol. 19, No. 5, 1990, pp. 1179–1232. doi:10.1063/1.555867.

[56] Kestin, J., Knierim, K., Mason, E., Najafi, B., Ro, S., and Waldman, M., “Equilibrium and Transport Properties of the Noble Gases and their Mixtures at Low Density,” Journal of Physical and Chemical Reference Data, Vol. 13, No. 1, 1984, pp. 229–303. doi:10.1063/1.555703.

[57] Levin, E., and Wright, M. J., “Collision Integrals for Ion-neutral Interactions of Nitrogen and Oxygen,” Journal of Thermophysics and Heat Transfer, Vol. 18, No. 1, 2004, pp. 143–147. doi:10.2514/1.2552.

[58] Bourdon, A., and Vervisch, P., “Study of a Low-pressure Nitrogen Plasma Boundary Layer over a Metallic Plate,” Physics of Plasmas, Vol. 4, No. 11, 1997, pp. 4144–4157. doi:10.1063/1.872535.

[59] Moran, T., Flannery, M., and Cosby, P., “Molecular Charge Transfer. II. Experimental and Theoretical Investigation of the Role of Incident-ion Vibrational States in O 2+–O 2 and NO+–NO Collisions,” The Journal of Chemical Physics, Vol. 61, No. 4, 1974, pp. 1261–1273. doi:10.1063/1.1682048.

[60] McBride, B., Zehe, M., and Gordon, S., “NASA Glenn Coefficients for Calculating Thermodynamic Properties of Individual Species (NASA\TP-2002-211556),” Cleveland: Glenn Research Center, 2002.

[61] Millikan, R. C., and White, D. R., “Systematics of Vibrational Relaxation,” The Journal of Chemical Physics, Vol. 39, No. 12, 1963, pp. 3209–3213. doi:10.1063/1.1734182.

[62] Park, C., “Assessment of Two-temperature Kinetic Model for Ionizing Air,” Journal of Thermophysics and Heat Transfer, Vol. 3, No. 3, 1989, pp. 233–244. doi:10.2514/3.28771.

[63] Moses, R. W., Cheatwood, F. M., Johnston, C. O., Macheret, S. O., Parent, B., Little, J., Williams, R., Green, J. S., Austin, M., and Aldrin, A., “New MHD Lift Concept for More Efficient Missions to Mars and Neptune,” AIAA SCITECH 2022 Forum, 2022, p. 0934. doi:10.2514/6.2022-0934.

[64] Anderson, J. D., Hypersonic and High Temperature Gas Dynamics, American Institute of Aeronautics and Astronautics, Reston, VA, 1989.

[65] Tabuchi, K., and Fujino, T., “Characteristics of Radiative Heating in Mars Entry Flight with Magnetohydrodynamic Flow Control,” AIAA AVIATION 2023 Forum, 2023, p. 4024. doi:10.2514/6.2023-4024.